Contents lists available at ScienceDirect

Arabian Journal of Chemistry

journal homepage: www.ksu.edu.sa

Original article

Zea mays bracts extract as an eco-friendly corrosion inhibitor for steel in HCl pickling solution: Experimental and simulation studies

Jia-hao Zhu [a], Bi-lan Lin [a,*], Tian-hu Duan [a], Han-quan Lin [a], Guo-yu Zhang [a], Xin-xin Zhou [a], Yu-ye Xu [b,*]

[a] *School of Material Science and Engineering, Xiamen University of Technology, No. 600 Ligong Road, Jimei District, Xiamen, Fujian Province, China*
[b] *College of Civil Engineering, Huaqiao University, No. 668 Jimei Avenue, Jimei District, Xiamen, Fujian Province, China*

ARTICLE INFO

Keywords:
Plant corrosion inhibitor
Zea mays bracts
Ultrasonic extraction
UPLC-QTFMS
Mild steel

ABSTRACT

Active phytochemicals with unique electron structures can adsorb on metal surfaces and effectively mitigate metal corrosion. Recently, plant extracts have garnered significant attention as green and renewable corrosion inhibitors. In this study, the abundant agricultural byproducts, namely *Zea mays* bracts, were used as the extract raw materials, and *Zea mays* bracts extract (ZMBE) was served as an eco-friendly corrosion inhibitor for mild steel (MS) in 1 M HCl pickling solution. The organic substances in ZMBE were analyzed via ultra-high performance liquid chromatography- quadrupole time-of-flight mass spectrometry (UPLC-QTFMS). The interaction between the active functional groups and MS was investigated using Fourier transform infrared (FT-IR) and ultraviolet–visible (UV–visible) spectroscopy and X-ray photoelectron spectroscopy (XPS). The corrosion inhibition behavior was scrutinized through potentiodynamic polarization (PDP) curves and electrochemical impedance spectroscopy (EIS). The results show that functional groups such as aromatic rings, double bonds, and hydroxyls successfully adsorb on the MS surface to form the protective films. ZMBE exhibits a mixed-type corrosion inhibition with a “geometric coverage” effect. The corrosion inhibition efficiency (η) increases with ZMBE concentration and solution temperature, the optimum η with 5.0 $g{\cdot}L^{-1}$ ZMBE at 318 K is 96.2 %. The adsorption of active ingredients follows the Langmuir and El-Awady isotherms. Density functional theory (DFT) and molecular dynamics (MD) simulations prove the synergistic effect of complex components in ZMBE and the corrosion inhibition mechanism. ZMBE is a promising acid pickling corrosion inhibitor with broad application prospects.

1. Introduction

Mild steel (MS), characterized by a carbon content of less than 0.25 %, serves various purposes in the fabrication of pipes, plates, rods, wires, profiles, etc. Recognized for its excellent machinability, high strength and hardness, good ductility, and low cost, MS has been widely used in construction, infrastructure, automotive industry, machinery manufacturing, petrochemicals, and other fields (El-Labban et al., 2016; Paul et al., 2014). However, MS is highly susceptible to oxidation and corrosion in humid, oxygen-containing, or chlorinated environments. It not only results in serious resource wastage, but also poses safety hazards and risks. It’s estimated that approximately 30 % of metal equipment and materials worldwide are scrapped due to corrosion annually (Bender et al., 2022).

Currently, electrochemical protection, environmental control and protective coatings are three primary and widely adopted methods for safeguarding metals against corrosion. Acid pickling, due to the ability to swiftly and effectively eliminate rust and scales from metal surfaces, stands as one of the crucial pre-treatment processes for implementing coverage protection (Nadi et al., 2019). HCl solution is currently one of the most commonly used pickling solution owing to fast cleaning speed, strong ability to suppress acid mist, less susceptibility to hydrogen embrittlement, and no need for heating (Devi et al., 2014). Nevertheless, an ideal pickling solution should also exhibit minimal corrosive impact on the base metal (Sun et al., 2023a). Therefore, adding efficient corrosion inhibitor is one of the essential conditions. Plant corrosion inhibitors are the active organic substances extracted from various parts of plants such as roots (Thakur et al., 2022; Zhou et al, 2023), stems (Wang et al., 2023a), leaves (Harb et al., 2020), seeds (Deyab et al., 2022), flowers (Shahini et al., 2021), and fruit peels (Obuebite et al., 2022). Compared with synthetic corrosion inhibitors, these natural inhibitors have many advantages such as low cost, wide availability,

---

* Corresponding authors.
E-mail addresses: linbilan@xmut.edu.cn (B.-l. Lin), yuyexu@hqu.edu.cn (Y.-y. Xu).

https://doi.org/10.1016/j.arabjc.2024.105895
Received 27 March 2024; Accepted 3 July 2024

renewability, low toxicity, harmlessness, environmental friendliness, easy bio-degradation, simple extraction processes, and minimal residues (Shahini et al., 2021). Therefore, the exploration of natural corrosion inhibitors has become one of the key research directions for developing green corrosion inhibitors.

Plant extracts contain plentiful active ingredients such as sugars, alcohols, terpenes, phenols, ketones, organic acids (Dutta et al., 2017). These components possess unique molecular structures and can interact with metals through charge sharing and/or electrostatic attraction, adsorbing on the metal surface and providing corrosion protection (Thanh et al., 2020). The type and quantity of organic components in plant extracts are related to the plant type and extraction process (Zeng et al., 2023). Likewise, the corrosion inhibition effectiveness and adsorption behaviors of plant extracts exhibit obvious difference depending on the corrosion media and metals (Lin et al., 2021a). Currently, extensive research has been conducted on plant extracts as corrosion inhibitors. *Pomelo* peel extract (PPE) was used as a corrosion inhibitor for MS in 1 M H_3PO_4 solution, the adsorption of active molecules on the MS surface followed the Langmuir isotherm. Oxygenated heterocycles and unsaturated C═O bonds in PPE could chelate with Fe^{2+} and coordinate with Fe atoms, forming an adsorption film to inhibit corrosion (Lin et al., 2021a). The adsorption of *Dryopteris cochleata* leaves extract on aluminum surface in 1 M H_2SO_4 solution followed the Freundlich isotherm. A protective film was formed by the chemical interaction between aluminum and π-electrons in extract and by the physical adsorption (Nathiya and Raj, 2017). *Borage* flower extract in 1 M HCl solution obstructed the corrosion of the MS active sites through chemical adsorption and primarily served as a mixed-type corrosion inhibitor (Dehghani et al., 2019a). *Garcinia indica* (*Binda*) extract also acted as a mixed-type corrosion inhibitor, but the protective film was achieved through physical adsorption by electrostatic attraction between the aromatic rings and the positively-charged MS surface (Thomas et al., 2020). *Zizyphus Lotuse* extract interacted with copper surface through physical adsorption, and was a cathodic corrosion inhibitor in HCl solution (Jmiai et al., 2018).

Zea mays belongs to the *Poaceae* family, known as maize, bract, pearl rice, etc. *Zea mays* is renowned as a nutritious health food among coarse grains. Similar to *Zea mays*, its bracts also contain various phytochemicals such as flavonoids (Fernandez-Aulis et al., 2019; Kisa, 2016; Tian et al., 2016), carbohydrates (Ratna et al., 2023; Tachaapaikoon et al., 2006), phenolic compounds (Vazquez-Olivo et al., 2019; Capocchi et al., 2017), phenylpropanoids (Li et al., 2013a; Kopsell et al., 2011). These organic compounds are rich in heterocycles, benzene rings, hydroxyls, carboxyls, carbonyls, double bonds, etc. It is anticipated to interact with metals and form a protective film, reducing the contact between the metal surface and the corrosive medium. Therefore, the extract from *Zea mays* bracts holds the potential to serve as an effective, non-toxic and economic corrosion inhibitor for metals in corrosive environments.

Nevertheless, *Zea mays* bracts, as the agricultural by-products during harvest, are often disposed of through burial or burning, causing serious environmental burden and greenhouse effect, which is not conducive to achieving the world's carbon reduction goals. The use of *Zea mays* bracts as a raw material can not only alleviate the environmental pollution, but can also contribute to the development of new environmentally friendly, widely sourced and cost-effective corrosion inhibitors. *Zea mays* bracts are more biodegradable than the traditional synthetic corrosion inhibitors. Moreover, the preparation process of plant extracts is relatively simple and easy to operate. It helps to simplify the production process, reduce costs, improve the feasibility of practical applications, aligning with the concept of sustainable development.

Recently, research on *Zea mays* bracts has predominantly focused on their medicinal and agricultural value, while little attention has been paid to their potential as corrosion inhibitors. Corn cob extract was used as the corrosion inhibitor for aluminum alloy in 1.0 M H_2SO_4 (Echem et al., 2023). The results showed that the average corrosion rate decreased as the extract concentration increased, and a multilayered film was formed (Echem et al., 2023). Mathur et al. (Mathur et al., 2023) obtained the multi-layer films by repeatedly dripping and drying ethanol extract of corn husk leaves (EECH). The results showed that the smoothness and uniformity of the MS surface were enhanced and the impedance of MS with a three-layer EECH film was approximately twice that of the bare MS. Therefore, further exploration and utilization of extracts from corn agricultural and sideline products to improve metal corrosion resistance is of great significance.

In this article, the organic active ingredients were extracted from *Zea mays* bracts, denoted as ZMBE, and were utilized as eco-friendly corrosion inhibitor for MS in 1 M HCl pickling solution. The organic substances and the functional groups in ZMBE were analyzed via UPLC-QTFMS, FT-IR and UV–visible spectra. The chemical compositions of the adsorption film on the MS surface were studied by XPS, and the corrosion morphology was observed using scanning electron microscope (SEM). The corrosion inhibition behavior of ZMBE was investigated through electrochemical tests. The adsorption isotherms and parameters were delved. To gain insights into the adsorption behavior of the active ingredients at the atomic level, DFT and MD calculations were conducted. And the corrosion inhibition mechanism was revealed.

2. Experimental

2.1. Preparation of Zea mays bracts extract

Fresh *Zea mays* bracts collected from an agricultural trade market in Xiamen of China were cleaned and placed in the shade to dry water stains. After drying in an oven at 353 K, they were crushed and passed through a 60-mesh sieve to remove the coarse particles.

Adhering to the principle of "similarity and intermiscibility", an ethanol aqueous solution (ethanol: water = 4:1 v/v%) was chosen as the extraction solvent. The ultrasonic-assisted leaching method with cavitation, activation and mechanical effects was employed to promote the dissolution of the active ingredients. The extraction process involved thoroughly mixing an appropriate amount of *Zea mays* bracts powder with the extraction solvent, followed by placement in an ultrasonic machine at 313 K for 4 h. The upper mixed solution was filtered to remove the undissolved residues, and then the filtrate was concentrated at a vacuum rotary evaporator. Meanwhile, the ethanol extraction solvent was recovered. Finally, the super-concentrated solution was thoroughly dried in an oven at 353 K, and the amber colloidal substance, i.e. *Zea mays* bracts extract (ZMBE), was obtained.

2.2. Materials and corrosion solution

The chemical compositions of MS used were as follows (wt.%): 0.13C, 0.02Si, 0.38 Mn, 0.014P, 0.031 S, and balance Fe. The sample dimension for electrochemical and microscopic analysis was 10 mm × 10 mm × 2 mm, that for XPS analysis was 5 mm × 5 mm × 2 mm.

The corrosion environment was a 1 M HCl solution, derived from a 36.5 wt% hydrochloric acid. To explore the corrosion inhibition behavior and adsorption model of ZMBE, the influence of the ZMBE concentration and the solution temperature was considered. The added ZMBE concentration was 0, 0.1, 0.5, 1.0, 3.0 and 5.0 $g \cdot L^{-1}$, respectively. And the temperature of 1 M HCl solution was 298, 308, and 318 K, respectively.

2.3. Electrochemical measurements

For the MS sample, a specific surface area of 10 mm × 10 mm was chosen as the working surface. On the reverse surface, a copper wire conductor was soldered and subsequently encased with three layers of heat-shrink tubing. Except for the designated working surface (1.0 cm^2 area), all components including welded joints were encapsulated with epoxy resin to prevent galvanic corrosion. The working surface was polished using waterproof sandpapers ranged from No. 400# to No.

2000#, followed by scrubbing with ethanol, rinsing with distilled water, and drying with cold air. The working electrode was obtained.

The electrochemical measurements were carried out under a CS310H workstation (Corrtest Instrument Corp., Ltd. Wuhan, China). A conventional three-electrode system, i.e. the tested MS electrode as the working electrode, a platinum electrode as the auxiliary electrode, and a saturated calomel electrode (SCE) as the reference electrode, was used. Before electrochemical measurements, the open circuit potential (OCP) should be monitored to determine the dynamic equilibrium state of the corrosion system and to acquire a nearly stable OCP value. The OCP test time was 1 h to ensure the consistency of the experiments and the reliability of the results.

EIS test was conducted at the stabilized OCP. The AC signal amplitude was 10 mV, and the frequency spanned from 100 kHz to 0.01 Hz. Based on the shape of the EIS diagrams and the characteristic of the corrosion system, a suitable equivalent circuit was constructed, and the EIS data was fitted using Zview software.

Following the EIS test, the PDP curve was measured. The polarization potential was set at ± 0.3 V vs. OCP, and a common scan rate of 1 $mV\cdot s^{-1}$ was employed.

To ensure the reproducibility and reliability of the electrochemical results, three parallel tests were conducted for each condition. In the present corrosion system, the electrochemical results of three parallel tests were almost identical, so the error range was not provided below.

2.4. UPLC-QTFMS analysis

The organic compounds in ZMBE were analyzed using UPLC-QTFMS referred to our previous study (Lin et al., 2023b).

2.5. FT-IR spectroscopy analysis

A polished and cleaned MS sample was immersed in 1 M HCl solution containing 5.0 $g\cdot L^{-1}$ ZMBE for 3 h and the corrosion products including ZMBE adsorption film were formed on the MS surface. Then the corrosion products were scraped off, mixed with KBr and ground evenly. A tablet was pressed. Similarly, the ZMBE colloid was mixed with KBr, ground uniformly and made into tablet. The FT-IR spectra of the above two tablets which were fully dried were recorded with an ALPHA FT-IR spectrometer (Bruker Corporation, Germany). The wavenumber was in the range of 400–4000 cm^{-1}. The functional groups in organic extract were analyzed and the adsorption of the organic substances on the MS surface was judged (Shahid et al., 2018).

2.6. UV–visible spectroscopy analysis

A 1 M HCl corrosion solution containing 5.0 $g\cdot L^{-1}$ ZMBE was divided into two distinct portions. In one part, a polished and cleaned MS sample was immersed for 24 h, denoting this corroded solution as “after immersion”. The second part, untouched by MS, was labeled as “before immersion”. Subsequently, UV–visible spectra were analyzed using a UV-2700 UV–visible spectrometer (Shimadzu, Japan). The wavelength ranged from 200 to 800 nm, with a scanning interval of 1 nm. Deionized water was served as the reference solution (Akash and Rehman, 2020).

2.7. XPS analysis

A polished and cleaned MS sample was immersed in 1 M HCl solution with 5.0 $g\cdot L^{-1}$ ZMBE for 3 h and then was thorough rinsed with deionized water and dried with cool air. An AXIS SUPRA + X-ray photoelectron spectrometer (Shimadzu, Japan) was employed to measure the full XPS spectrum of the MS surface, and the element compositions were judged. Subsequently, the high-resolution XPS spectra for each element were collected. After peak fitting, the presence forms of the element were determined. This detailed characterization was profit to assess the adsorption of organic components on the MS surface.

2.8. Surface observation

In order to more intuitively reflect the corrosion inhibition of ZMBE on MS, the surface observation was conducted. Similarly, the polished and thoroughly cleaned MS samples were immersed in 1 M HCl solution without ZMBE and with 1.0 and 5.0 $g\cdot L^{-1}$ ZMBE for 3 h, respectively. The subsequent cleaning process was similar to that described in XPS analysis. The corroded MS sample was acquired. A field emission SEM (Sigma 500, Germany, EHT = 15 kV) was invited to observe the surface corrosion morphology.

3. Theoretical calculations

3.1. DFT simulations

To explore the electronic stability and chemical reactivity of the active ingredients in ZMBE, DFT calculations were conducted using Gaussian 16 software. The geometrically balanced configurations of the neutral molecules, characterized by the non-magnetic and non-electrical nature, were fully optimized based on the 6-311G**(d, p) basis group and the B3LYP method (Lin et al., 2024c; Zhao et al., 2023). In acidic media, some heteroatoms with more negative electrons in the organic molecules will capture hydrogen ion and protonate. The protonated molecules, i.e. onium ions, were positively charged. The protonation of active ingredients may affect the electronic stability and adsorption behavior. Therefore, the geometric optimization at different protonated positions for each active molecule was performed and the optimal protonated equilibrium configuration was gained. Water was used as the simulated solvent (Khadom et al., 2021). The frontier molecular orbital distributions and the quantum chemical parameters for each equilibrium configuration molecule in both neutral and protonated states were calculated. The chemical stability, electron sharing abilities, adsorption behavior, etc. were evaluated.

3.2. MD simulations

To comprehend the corrosion inhibition performance of active molecules in ZMBE, it was crucial to investigate the adsorption mode and binding strength on the metal surface. MD simulations were performed for both neutral and protonated ingredients using Materials Studio 8.0 software. The Forcite module was utilized. The Fe (1 1 0) plane, because of the lowest thermodynamic energy (i.e. the most stable), was selected as the adsorption surface. The height of the vacuum layer was 30 Å. The crystal cell was $2.48 \times 2.48 \times 5.02\ nm^3$. 500 water molecules were filled in the vacuum layer, and one organic molecule was stuffed between water molecules and Fe atoms. The COMPASS force field was chosen to represent the interactions within the system. The temperature of the system was controlled using the Andersen Thermostat, and the system was regulated under NVT conditions. The calculation time was 500 ps, and the step size for each iteration was 1 fs (Melian et al., 2023).

4. Results and discussion

4.1. Chemical composition analysis results

4.1.1. UPLC-QTFMS results

Fig. 1 shows the UPLC-QTFMS chromatogram of ZMBE under the positive ion mode, and Table 1 presents the corresponding tentative identification results. ZMBE contains various phytochemicals such as carbohydrates (1: rhamnose, 2: ribose, 3: glucuronic acid, 4: glucose, 6: fucose (Tachaapaikoon et al., 2006), and 7: hemicellulose (Scheller and Ulvskov, 2010)), phenolic compounds (5: hydroxycinnamic acid (Vazquez-Olivo et al., 2019), 11: β-sitosterol, and 12: ergosterol (Capocchi et al., 2017)), phenylpropanoids (8: dimboa (Li et al., 2013a), 13: cryptoxanthin, 14: β-carotene, and 15: lutein (Kopsell et al., 2011)),

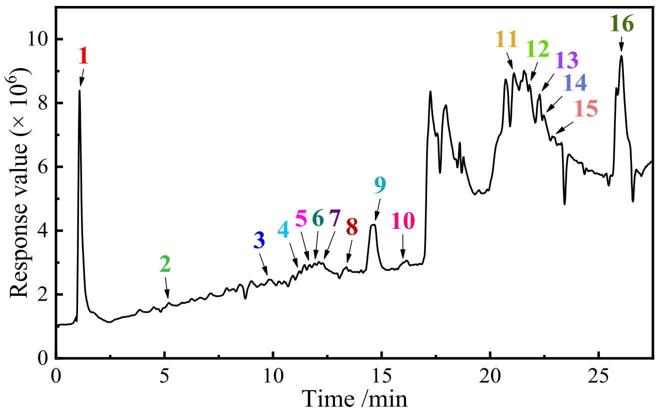

Fig. 1. UPLC-QTFMS chromatogram of ZMBE in the positive ion mode.

flavonoids (9: anthocyanins (Fernandez-Aulis et al., 2019), 10: tricin (Tian et al., 2016), and 16: rutin (Kisa, 2016)).

The active ingredients in ZMBE are exceedingly complex, and it is impractical to present the simulation results for all identified components. The ingredients were categorized into four groups. As an illustrative representation, one result of each group was showcased. Where hydroxycinnamic acid, dimboa, glucuronic acid, and rutin are the representatives of phenolic, phenylpropanoids, carbohydrates, and flavonoids, respectively. The molecular structures are shown in Fig. 2.

4.1.2. FT-IR spectroscopy results

Fig. 3 depicts the FT-IR spectra of ZMBE solid and the ZMBE adsorption film formed on the MS surface. As shown in Fig. 3a, a broad absorption band around 3274 cm^{-1} corresponds to the stretching vibration of –OH and –NH$_2$, confirming the presence of alcoholic compounds and carboxylic acids in ZMBE (Erfan and Mardali, 2024). The absorption peak at 2915 cm^{-1} corresponds to the stretching vibration of the saturated C–H bonds (Mourya et al., 2014). The absorption peak at 1634 cm^{-1} can be attributed to the stretching vibration of C=C and C=O in aromatic ring conjugated systems (Jokar et al., 2016), which are present in dimboa, rutin, and hydroxycinnamic acid. The absorption peak at 1342 cm^{-1} is corresponding to the symmetric stretching vibration of –COOH (Dehghani et al., 2019a). The absorption peak at 1248 cm^{-1} is due to the stretching vibration of C-O in aromatic ethers (Abdullah et al., 2023; Chen et al., 2023; Qiang et al., 2018), while the peak at 1008 cm^{-1} is associated with the stretching vibration of C-O in aliphatic ethers (Wu et al., 2020a). The absorption peaks observed below 1000 cm^{-1} are indicative of the bending vibrations of C–H in benzene rings or heterocycles (Fernandes et al., 2019; Wu et al., 2020a). It implies that ZMBE contains various functional groups, including –OH,

Table 1
UPLC-QTFMS data and tentative identification of the organic compounds in ZMBE.

Peak	Retention time/min	Molecular formula	Experimental *m/z*	Theoretical *m/z*	Δ*ppm*	Tentative identification
1	1.11	$C_6H_{14}O_6$	182.0790	182.0784	0.6	Rhamnose
2	5.79	$C_5H_{10}O_5$	150.0528	150.0547	−1.9	Ribose
3	9.95	$C_6H_{10}O_7$	194.0427	194.0475	−4.8	Glucuronic acid
4	11.15	$C_6H_{12}O_6$	180.0634	180.0635	−0.1	Glucose
5	11.77	$C_9H_8O_3$	164.0473	164.0482	−0.9	Hydroxycinnamic acid
6	11.78	$C_6H_{12}O_5$	164.0685	164.0693	−0.8	Fucose
7	12.19	$C_{12}H_{20}O_{10}$	324.1053	324.1014	3.9	Hemicellulose
8	13.61	$C_9H_9NO_5$	244.0481	244.0434	4.7	Dimboa
9	15.03	$C_{15}H_{11}ClO_6$	322.0244	322.0229	1.5	Anthocyanins
10	15.48	$C_{17}H_{14}O_7$	331.0812	331.0851	−3.9	Tricin
11	21.18	$C_{29}H_{50}O$	414.3862	414.3868	−0.6	*β*-sitosterol
12	21.91	$C_{28}H_{44}O$	396.3392	396.3376	1.6	Ergosterol
13	22.35	$C_{40}H_{56}O$	552.4331	552.4337	−0.6	Cryptoxanthin
14	22.55	$C_{40}H_{56}$	536.4832	536.4803	2.9	*β*-carotene
15	22.72	$C_{40}H_{56}O_2$	568.4280	568.4285	−0.5	Lutein
16	25.11	$C_{27}H_{30}O_{16}$	610.1534	610.1552	−1.8	Rutin

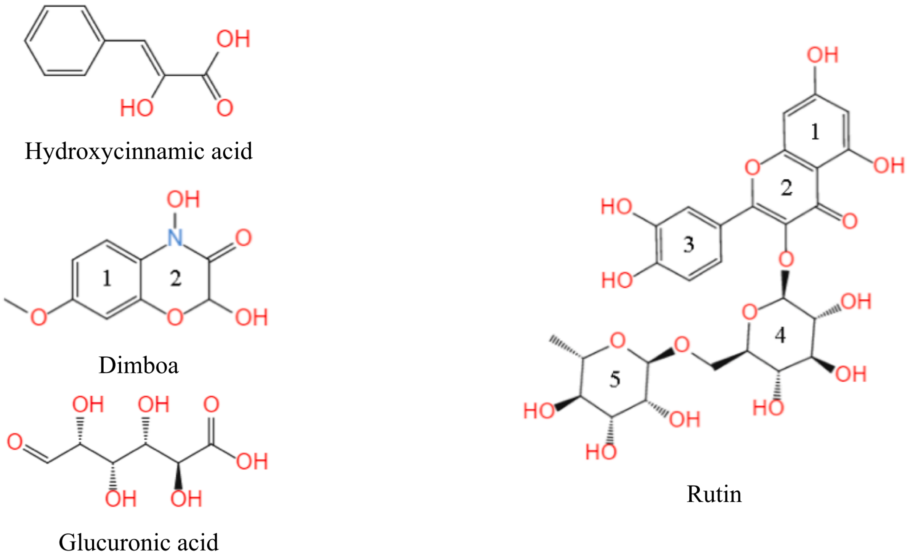
Hydroxycinnamic acid
Dimboa
Glucuronic acid
Rutin

Fig. 2. Molecular structures of some active ingredients in ZMBE.

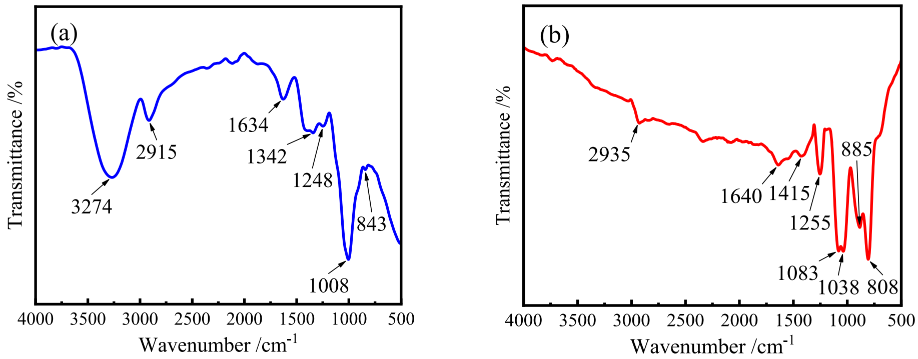

Fig. 3. FT-IR spectra: (a) ZMBE solid, and (b) ZMBE adsorption film on the MS surface.

–COOH, C═C, C═O, C–O, and aromatic rings, etc. These functional groups possess distinctive electronic structures, enabling them to share electrons with Fe atoms. They may also undergo chelation reactions with Fe ions and/or generate physical adsorption effects. Consequently, the active ingredients in ZMBE are adsorbed onto the surface, forming a protective adsorption film.

As shown in Fig. 3b, the broad absorption peak associated with the stretching vibration of –OH and $–NH_2$ in the adsorption film is significantly reduced. It suggests that the –OH bonds in ZMBE are chelated with Fe atoms or ions and the $–NH_2$ bonds may share electrons with iron atoms, forming iron complexes. However, the position and quantity of the absorption peaks, corresponding to the characteristic groups present in ZMBE, remain nearly identical in both spectra. It further confirms that the organic substances in ZMBE have successfully adsorbed onto the MS surface, playing a crucial role in inhibiting the corrosion of MS.

4.1.3. UV–visible spectroscopy results

Fig. 4 shows the UV–visible spectra of 1 M HCl solution with 5.0 $g{\cdot}L^{-1}$ ZMBE before and after immersion of MS samples. Before immersion, the absorption peak at 224 nm corresponds to the π-π* transition of the C═C bonds in aromatic rings. It indicates that ZMBE has the aromatic compounds, which own unsaturated bonds and π electrons and form a conjugated closed system (Prasad et al., 2023a). The absorption peak at 284 nm is attributed to the n-π* transition of the $C = O$ bonds in carbonyl compounds (Sığırcık et al., 2017). After immersion, the absorbance intensity at the same wavelength regions decreases, and the two peaks are slightly blue-shifted to 222 and 282 nm, respectively. It can be concluded that the C═C and C═O bonds in ZMBE interact with the MS surface through physical adsorption and chemical adsorption and form the stable complexes with Fe ions in the solution (Fergachi et al., 2019; Goel et al., 2010; Sığırcık et al., 2017).

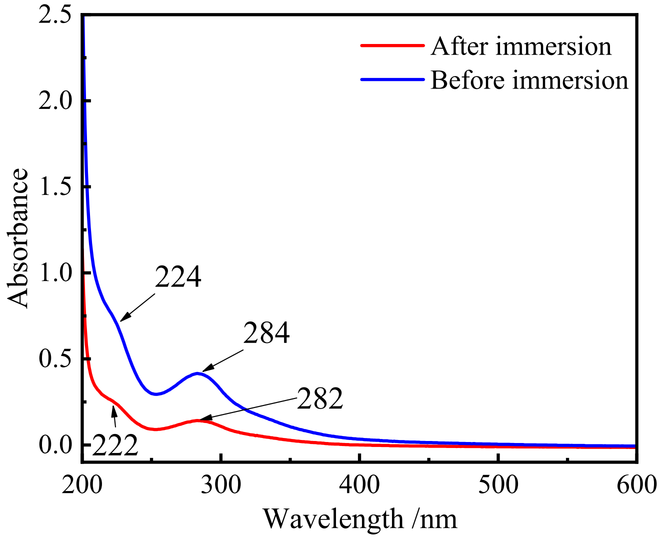

Fig. 4. UV–visible spectra of 1 M HCl solution with 5.0 $g{\cdot}L^{-1}$ ZMBE before and after immersion of MS sample.

4.1.4. XPS results

To further understand the adsorption and corrosion inhibition behavior of the phytochemical components on the MS surface, their existing forms were investigated. The XPS full-spectrum shows the presence of C, N, O and Fe in the adsorption film. The high-resolution XPS spectra and the peak fitting results of these four elements are shown in Fig. 5.

As shown in Fig. 5a, the C 1 s spectrum in the adsorption film can be divided into three types of substances. The absorption peak at 284.8 eV corresponds to the C═C, C–C and C–H bonds in aromatic rings (El-Azzouzi et al., 2022), which may originate from the active ingredients such as hydroxycinnamic acid, dimboa, and rutin. The absorption peak at 285.6 eV is related to the C-N and $C\text{-}N^{+}$ bonds in organic molecules (Bouanis et al., 2016; Cunha et al., 2023). The former most likely originates from the neutral dimboa, amino acids, and other ingredients in ZMBE, while the latter may arise from the corresponding protonated molecules. The small peak at 288.4 eV is attributed to the C–O, C═O, $C–O^{+}$ and $C═O^{+}$ bonds (Du et al., 2023a). The first two bonds may originate from the neutral ingredients like hydroxycinnamic acid, dimboa, glucuronic acid, and rutin, while the latter two may be related to their protonated molecules. It is worth noting that there is no N element in MS, but the presence of C-N bonds confirms the adsorption of ZMBE on the MS surface.

As shown in Fig. 5b, the N element primarily exists in two forms. The peak at 399.8 eV corresponds to the C-N and $C\text{-}N^{+}$ bonds, and that at 400.4 eV is corresponding to the $–NH_2$ bond (Sun et al., 2022b). These may originate from dimboa or other amino acids in ZMBE.

As shown in Fig. 5c, the O element can be divided into three forms. The binding energy at 529.8 eV corresponds to the O 1 s in Fe_2O_3 and Fe_3O_4 (Mukhopadhyay et al., 2021). The strongest peak at 531.8 eV is corresponding to FeOOH and FeO (Hu et al., 2021a). The peak at 533.2 eV is related to the neutral C–O and C═O bonds and the protonated $C–O^{+}$ and $C═O^{+}$ bonds in organic substances (Attou et al., 2020). It further confirms the adsorption of the ZMBE's active ingredients on the MS surface. This is consistent with the C 1 s results.

As shown in Fig. 5d, the Fe $2p_{3/2}$ spectrum can be divided into three distinct peaks. The first peak at 706.5 eV corresponds to the metallic iron (Fe^{0}) (Ahmed and Zhang, 2020). It indicates that the coverage of the adsorption film of ZMBE is not 100 % and there are some defects. The strong and broad peak at 710.8 eV arises from oxygen elements in Fe_2O_3, FeOOH, FeO, and Fe_3O_4 (Berrissoul et al., 2022a; Hashim et al., 2019). The presence of FeOOH and Fe_2O_3 suggests that the addition of ZMBE favors the formation of denser and more stable Fe^{3+} compounds, which enhance the corrosion resistance. The small peak at 714.4 eV corresponds to the Fe complexes (Garai et al., 2012). This may be due to that

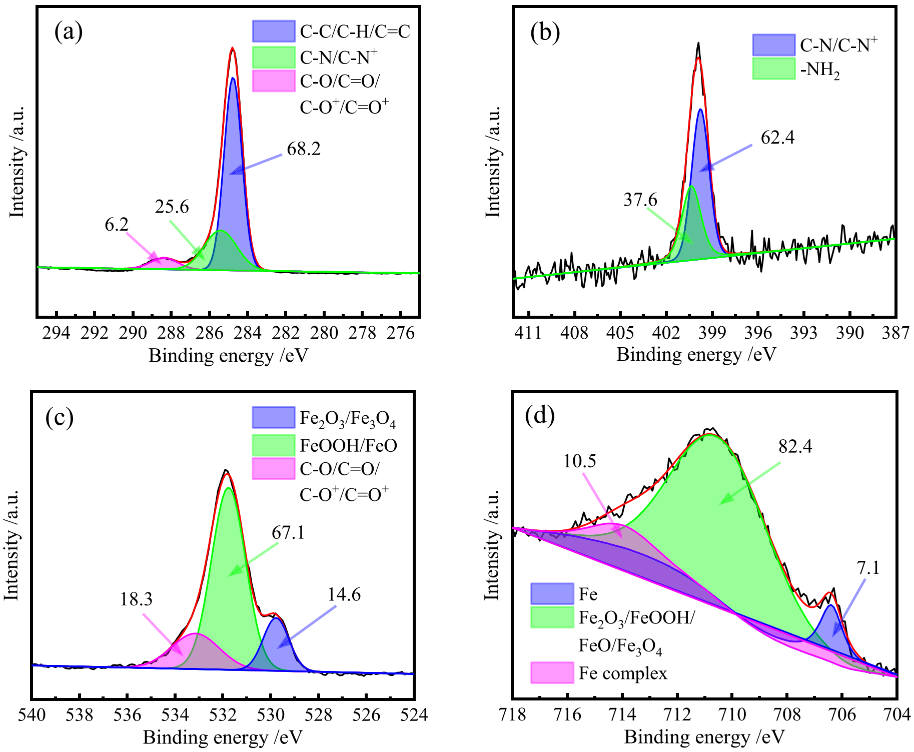

Fig. 5. High-resolution XPS spectra of elements in ZMBE adsorption film on the MS surface: (a) C 1 s; (b) N 1 s; (c) O 1 s; and (d) Fe $2p_{3/2}$.

the organic molecules in ZMBE act as electron donors and/or electron acceptors for Fe atoms, and it could also be owing to the chelation reactions between the adsorptive functional groups and Fe ions (Olivares-Xometl et al., 2006). The latter is consistent with the FT-IR results where the absorption peak of hydroxyl on the MS surface is almost disappeared.

The XPS analysis indicates that the active molecules in ZMBE can effectively adsorb on the MS surface, forming a protective film. It serves to reduce the contact between MS and corrosive media, thereby reducing the corrosion.

4.2. *Surface observation results*

Fig. 6 shows the surface morphology of MS samples immersed in 1 M HCl solution with different concentration of ZMBE. As shown in Fig. 6a, in the absence of ZMBE, the MS surface is corroded severely and the corrosion pits are densely distributed. A typical uniform corrosion is manifested. Upon the addition of 1.0 g·L^{-1} ZMBE, the corrosion pits are reduced noticeably, as shown in Fig. 6b. With a ZMBE concentration of 5.0 g·L^{-1}, the MS surface reveals the absence of corrosion pits, accompanied by the presence of a blurred protective film. It substantiates the effective corrosion inhibition of MS in 1 M HCl solution by ZMBE,

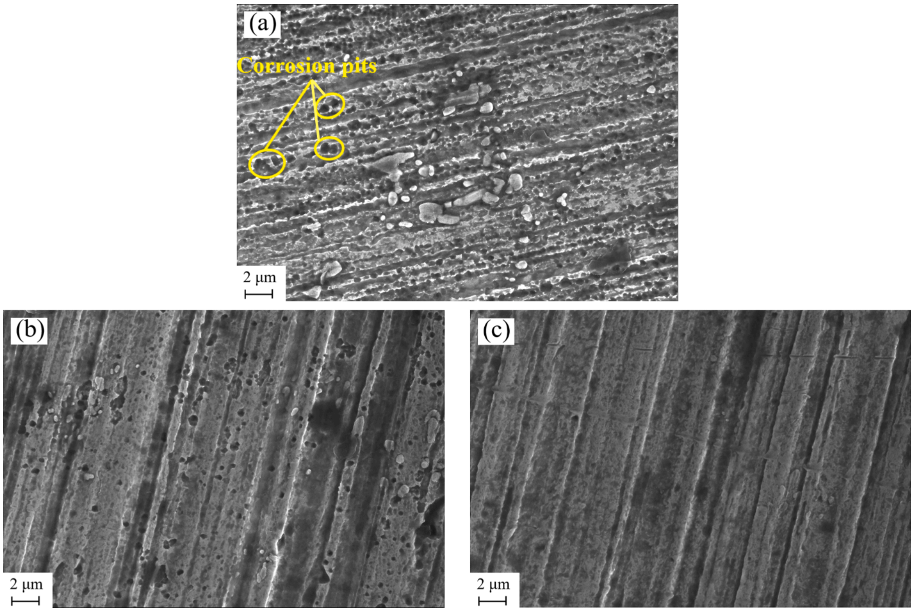

Fig. 6. Effect of ZMBE concentration on surface morphology of MS in 1 M HCl solution: (a) without ZMBE; (b) with 1.0 g·L^{-1}; and (c) with 5.0 g·L^{-1} ZMBE.

establishing it as an excellent and green corrosion inhibitor.

4.3. Electrochemical corrosion results

4.3.1. OCP curves

OCP is the common potential formed by mutual polarization between the anodic and cathodic equilibrium potential in a natural state. The shifts in OCP provide a means to evaluate the equilibrium tendencies of the electrode reactions (Li et al., 2021b).

Fig. 7 shows the OCP-time curves for MS in 1 M HCl solution with various concentration of ZMBE at 298, 308, and 318 K. In Fig. 7a, regardless of the presence or the absence of ZMBE in 1 M HCl solution at 298 K, the change trend of OCP with time is almost similar. There is a rapid increase in OCP during the initial 300 s of immersion, followed by a continuous decrease. Around 1500 s, the OCP is stabilized gradually, indicating that electrode reactions on the MS surface approach the dynamic equilibrium. Compared to the blank solution, the addition of ZMBE makes the OCP of MS shift in the negative direction by approximately 30–35 mV. However, only when the potential fluctuation range is greater than 85 mV, an anode-type or cathodic-type corrosion inhibitors can be judged (Moradia et al., 2021; Xu et al., 2024a). It suggests that ZMBE in 1 M HCl solution at 298 K behaves as a mixed-type corrosion inhibitor with a slightly dominant inhibition on cathodic reaction.

As illustrated in Fig. 7b and 7c, the OCP change law at 308 K closely mirrors that at 298 K. At 318 K, the change trend of OCP in the initial immersion stage is slightly different, but it stabilizes eventually. Similarly, the negative shift in the stable OCP with the addition of ZMBE at 308 and 318 K is consistently below 30 mV. It reaffirms the role of ZMBE as a mixed-type corrosion inhibitor for MS in 1 M HCl solution at 308 and 318 K. Moreover, the stabilization of OCP is more rapidly with increasing the solution temperature. This may be attributed to the organic components in ZMBE being more easily adsorbed onto the surface of MS at higher temperature.

4.3.2. PDP curves

Fig. 8 shows the PDP curves for MS in 1 M HCl solution with different concentration of ZMBE at 298, 308 and 318 K. Table 2 provides the corresponding polarization parameters. C_{inh} represents the concentration of ZMBE. E_{cor} and i_{cor} are the corrosion potential and corrosion current density of MS, respectively. b_c and b_a are the cathodic and anodic Tafel slope values, respectively. η_{PDP} is the corrosion protection efficiency of ZMBE for MS and was calculated by the corrosion current density without ZMBE (i^0_{cor}) and with ZMBE (i_{cor}) (Jero et al., 2023; Zaidi et al., 2023):

$$\eta_{\mathrm{PDP}} = \frac{i^0_{\mathrm{cor}} - i_{\mathrm{cor}}}{i^0_{\mathrm{cor}}} \times 100\backslash\% \tag{1}$$

As depicted in Fig. 8a, the addition of ZMBE to 1 M HCl solution at 298 K prompts the PDP curves shift downwards to the left. Both the anodic and cathodic polarization currents decrease, signifying the inhibition of both the anodic and cathodic corrosion reactions of MS. It can be ascribed to the adsorption of organic molecules on the MS surface, forming a protective film. Notably, the amplitude of the leftward shift in the cathodic curve surpasses that in the anodic curve, indicating a more pronounced inhibitory effect of ZMBE on the cathodic reaction. However, the negative shift of E_{cor} is clearly less than 50 mV, further supporting that ZMBE acts as a mixed-type corrosion inhibitor for MS in 1 M HCl pickling solution (Akounach et al., 2022).

As depicted in Fig. 8a, the addition of ZMBE does not significantly alter the shape of the PDP curves, indicating that the cathodic and anodic reactions of MS in 1 M HCl solution remain largely unchanged. Specifically, the hydrogen evolution at the cathode and the iron dissolution at the anode persist. In an acidic corrosion system governed by the activation polarization, the inhibitory mechanism of organic molecules can be attributed to the "geometric coverage" effect. Here, the adsorption film serves to isolate the metal surface from the acidic solution. Consequently, the electrode reactions are confined to the covered surface, while the uncovered portion continues to undergo the original corrosion reactions. With an escalation in ZMBE concentration, a greater number of active sites on MS are coated. It results in a reduction of the active areas and the cathodic and anodic reaction points. Consequently, there is a deceleration in reaction rates and a leftward shift in the polarization curves. The more pronounced leftward shift in the cathodic branch may be attributed to the more conspicuous adsorption behavior of organic substances on cathodic active sites. Besides chemical

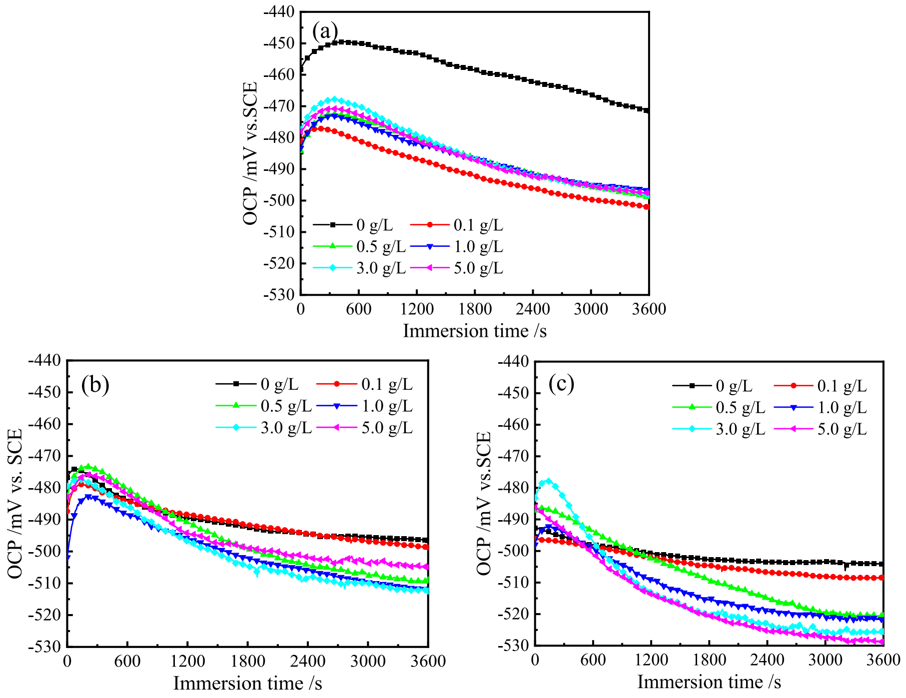

Fig. 7. OCP curves for MS in 1 M HCl solution with different content of ZMBE at (a) 298, (b) 308, and (c) 318 K.

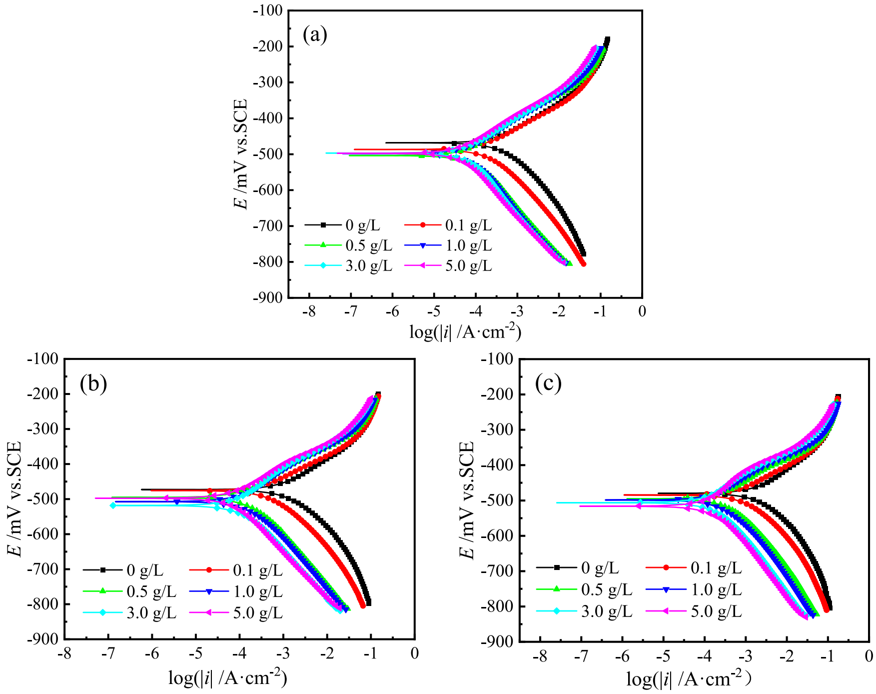

Fig. 8. PDP curves for MS in 1 M HCl solution with different content of ZMBE at (a) 298, (b) 308, and (c) 318 K.

Table 2
Effect of ZMBE content on PDP parameters for MS in 1 M HCl solution at different temperature.

T/K	C_{inh}/g·L^{-1}	E_{cor}/mV vs. SCE	b_c/mV·dec^{-1}	b_a/mV·dec^{-1}	i_{cor} ($\times10^{-5}$)/A·cm^{-2}	η_{PDP}/%	θ_{PDP}
298	0	−468	−129	87	43.87	–	–
	0.1	−487	−120	77	19.05	56.5	0.565
	0.5	−493	−108	75	7.18	83.6	0.836
	1.0	−498	−134	78	6.52	85.1	0.851
	3.0.	−497	−141	79	6.01	86.3	0.863
	5.0	−493	−128	77	5.40	87.7	0.877
308	0	−473	−132	102	136.42	–	–
	0.1	−475	−122	82	48.14	64.7	0.647
	0.5	−495	−116	75	20.63	84.9	0.849
	1.0	−507	−115	83	15.48	88.7	0.887
	3.0	−518	−120	92	8.38	93.9	0.939
	5.0.	−497	−125	74	7.04	94.8	0.948
318	0	−480	−153	114	252.31	–	–
	0.1	−480	−127	83	83.77	66.8	0.668
	0.5	−495	−118	74	37.23	85.2	0.852
	1.0	−498	−111	71	20.69	91.8	0.918
	3.0	−506	−112	75	12.04	95.2	0.952
	5.0	−516	−116	89	9.65	96.2	0.962

adsorption owing to electron-sharing, physical adsorption induced by electrostatic forces between the protonated molecules and metal surface also preferentially occurs on the cathodic sites.

As shown in Fig. 8b and 8c, the influence law of ZMBE on PDP curves at 308 and 318 K follows a similar pattern to that at 298 K. ZMBE still works as a mixed-type corrosion inhibitor for MS in 1 M HCl solution. The corrosion inhibition mechanism still is the "geometric coverage" effect. Therefore, the coverage of ZMBE on the MS surface (θ) is equal to the corrosion inhibition efficiency and can be expressed as (Fatima et al., 2020):

$$\theta = \frac{\eta_{\mathrm{PDP}}}{100} \tag{2}$$

As shown in Table 2, compared to the blank HCl solution without ZMBE, the maximum difference in E_{cor} at 298 K is 36 mV and that at 308 and 318 K is also far less than 85 mV. ZMBE functions as a mixed-type corrosion inhibitor for MS. At three experimental temperature, i_{cor} of MS decreases as the ZMBE concentration increases. Correspondingly, η of ZMBE increases with its concentration, and so is the coverage of ZMBE on the MS surface. The optimal concentration of ZMBE at three experimental temperature is 5.0 g·L^{-1}. The relevant maximum η at 298, 308, and 318 K is 88.7 %, 94.8 %, and 96.2 %, respectively. In addition, η increases with an elevation in solution temperature, although the magnitude of increase between 308 and 318 K is relatively modest. Properly elevating the medium temperature is beneficial for the adsorption of active ingredients on the MS surface, consistent with the OCP results. It is crucial to highlight that as the temperature of the HCl solution rises, i_{cor} and corrosion rate of MS undergo a noticeable increase. Therefore, reducing the temperature of the corrosive environment emerges as one of the pivotal factors in mitigating the corrosion rate of metals.

4.3.3. EIS diagrams

Fig. 9 presents the Nyquist and Bode diagrams for MS in 1 M HCl solution with different content of ZMBE at 298 K. Figs. 10 and 11 show the EIS diagrams at 308 and 318 K, respectively.

As depicted in Figs. 9-11, whether or not ZMBE is added to 1 M HCl solution at 298, 308, and 318 K, all Nyquist diagrams exhibit a single distorted capacitive arc. It corresponds to the double-layer capacitance at the MS/solution interface. The distortion in semicircular arc is due to the frequency dispersion effect caused by the non-uniformity of the actual double-layer capacitance. Furthermore, with an increase in ZMBE concentration, the size of the semicircular arc and the impedance value increase. The electrode reaction resistance of MS and the corrosion inhibition effect of ZMBE are improved.

As depicted in Fig. 9c, 10c, and 11c, under all experimental conditions, only one peak is displayed in the phase angle spectra, suggesting that there is only one time constant for the corrosion process at the metal/solution interface (Rathod et al., 2022). All negative phase angle peaks consistently are smaller than 90°. This is attributed to the inherent roughness and non-uniformity of the metal surface in the actual electrochemical system. As the concentration of ZMBE increases, both the negative phase angle peak and the half-width of the angle peak augments. It suggests a thickening in metal/solution interface layer, a reduction in double-layer capacitance, and an extension in frequency response time (Asfia et al., 2020; Singh et al., 2008). This may be related to the displacement of water molecules initially adsorbed on the metal surface by the active organic molecules. As the concentration of ZMBE rises, the adsorption and coverage of these active molecules intensify. In turn, it leads to a reduction in exposed area of MS, a thickening in double-layer, and a decrease in local dielectric constant. Additionally, at three experimental temperature, the modulus of the low-frequency impedance shows an upward trend with increasing ZMBE content (as shown in Fig. 9b, 10b, and 11b). It suggests a concurrent increase in charge transfer resistance for the corrosion reaction of MS.

As depicted in Figs. 9-11, the addition of ZMBE at three experimental temperature almost does not alter the initial shape of the EIS diagrams. The corrosion mechanism of MS is not changed, and the corrosion inhibition mechanism of ZMBE still is the "geometric coverage" effect. Notably, as the temperature of the HCl solution rises, the EIS parameters such as the radius of the capacitive arc, the modulus of the low-frequency impedance, the negative phase angle peak, and the half-width of the angle peak decrease. It indicates a reduction in corrosion resistance of MS with the increase of the solution temperature.

Fig. 12 shows the schematic diagram of the electrode/electrolyte interface model and the equivalent circuit for analyzing EIS data. Where R_s and R_{ct} are the solution resistance and the charge transfer resistance. CPE, constant phase element, represents the electric double-layer capacitance of the interface between MS and solution and is expressed as (Damej et al., 2023; Singh et al., 2008):

$$Z_{CPE} = \frac{1}{Y_0(j\omega)^n} \tag{3}$$

Where Y_0 is the auxiliary parameter related to the capacitance value. n indicates the deviation of the actual capacitance and ranges from 0 to 1 (Wang et al., 2024b). When n is 1, CPE behaves as an ideal flat-plate capacitor. When n is smaller than 1, CPE represents a distorted capacitance. ω is the angular frequency, and j stands for the imaginary unit. The electric double-layer capacitance (C_{dl}) was calculated using the formula proposed by Hsu and Mansfeld (Lima et al., 2020):

$$C_{dl} = Y_0 \cdot (\omega_{max})^{n-1} = Y_0 \cdot (2\pi f_{max})^{n-1} \tag{4}$$

Where ω_{max} is the characteristic angular frequency, and f_{max} is the characteristic frequency corresponding to the maximum imaginary part in Nyquist diagram.

Table 3 shows the fitting parameters of the EIS diagrams. Based on the EIS results, the corrosion inhibition efficiency (η_{EIS}) of ZMBE was calculated by the charge transfer resistance without ZMBE (R^0_{ct}) and with ZMBE (R_{ct}) (Gu et al., 2023; Zakaria et al., 2022):

$$\eta_{EIS} = \frac{R_{ct} \text{ - } R^0_{ct}}{R_{ct}} \times 100\% \tag{5}$$

Similarly, because of the "geometric coverage" effect, the coverage

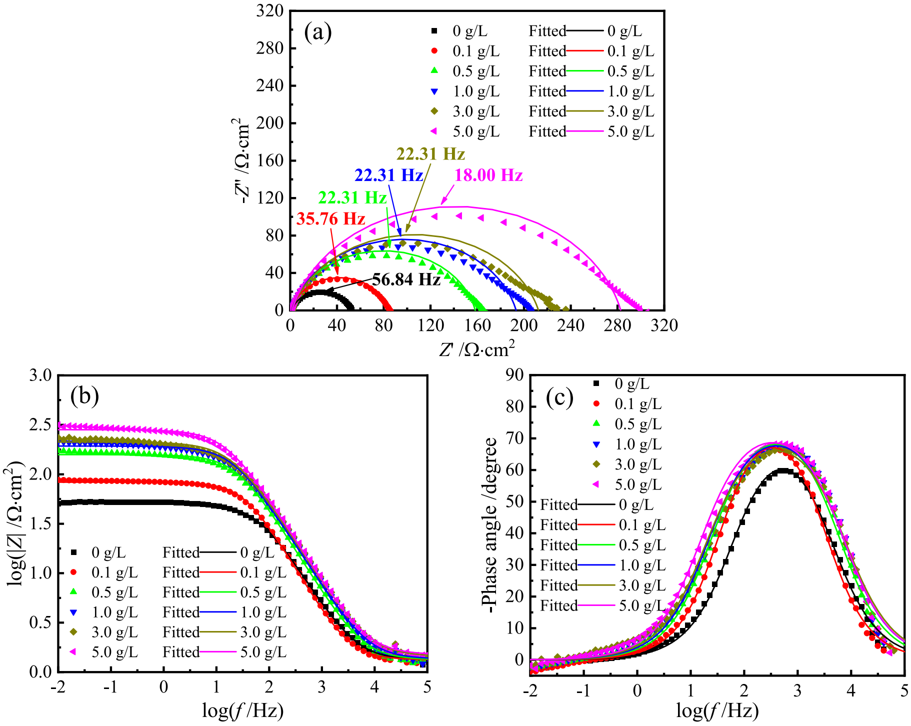

Fig. 9. EIS diagrams for MS in 1 M HCl solution with different content of ZMBE at 298 K: (a) Nyquist diagrams, (b) and (c) Bode diagrams.

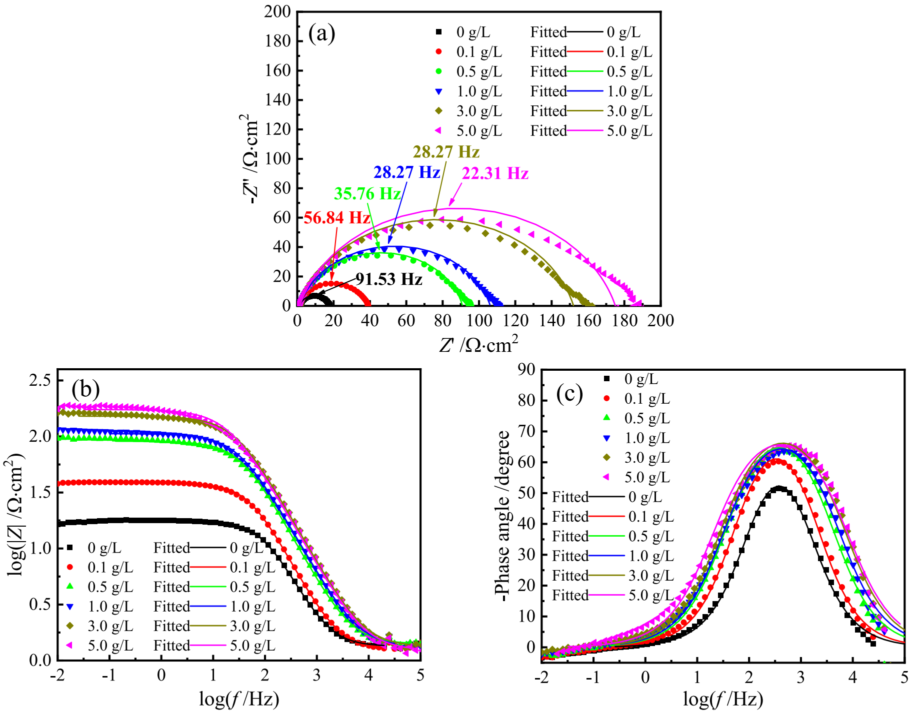

Fig. 10. EIS diagrams for MS in 1 M HCl solution with different content of ZMBE at 308 K: (a) Nyquist diagrams, (b) and (c) Bode diagrams.

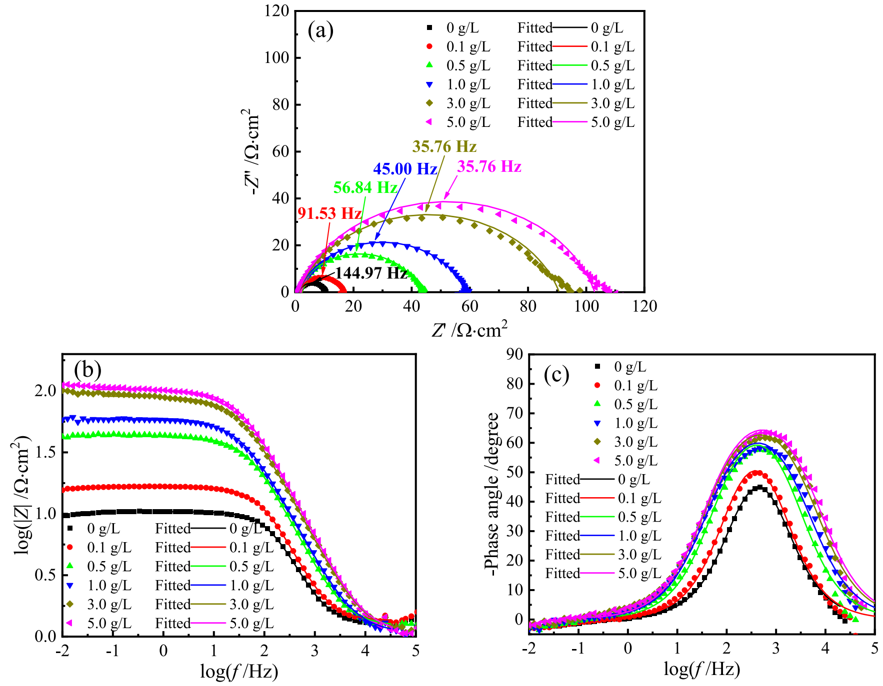

Fig. 11. EIS diagrams for MS in 1 M HCl solution with different content of ZMBE at 318 K: (a) Nyquist diagrams, (b) and (c) Bode diagrams.

of ZMBE based on EIS results (θ_{EIS}) is equal to the corrosion inhibition efficiency and was calculated by Eq. (2). As shown in Table 3, both ZMBE concentration and experimental temperature have little impact on the conductivity of the 1 M HCl solution, all R_s is around 1 Ω·cm^2. With an increase in ZMBE concentration, R_{ct}, η_{EIS}, and θ_{EIS} are significantly enhanced. The heightened concentration of active ingredients in the HCl solution promotes the adsorption and coverage on the MS surface. Consequently, the mechanical hindrance effect, the charge transfer resistance, and the overall corrosion inhibition effect are improved.

The value of n is related to the roughness and uniformity of the actual capacitance surface. A larger n means a closer the actual capacitance to an ideal flat-plate capacitor (Zuo et al., 2021). As indicated in Table 3, the addition of ZMBE has little impact on the value of n, which is within the range of approximately 0.81 to 0.90, approaching 1. It suggests that the electric double-layer at the MS/solution interface essentially behaves as an ideal flat-plate capacitor. The thin nature of the ZMBE adsorption film on the MS surface is likely responsible for this. It further confirms that all EIS diagrams exhibit only one capacitive arc and only

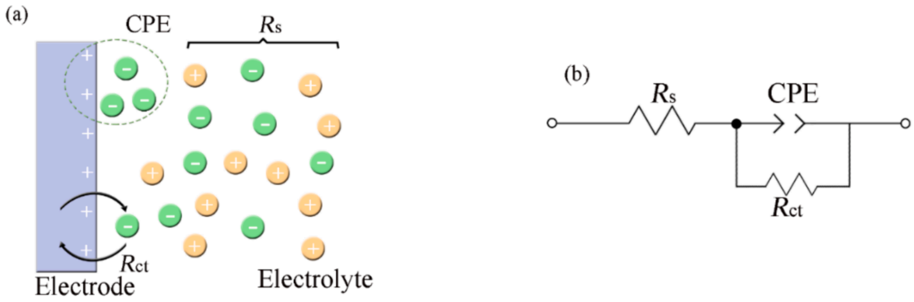

Fig. 12. (a) Schematic diagram of electrode/electrolyte interface, and (b) equivalent circuit for analyzing EIS data.

Table 3
EIS fitted parameters for MS in 1 M HCl solution with different concentration of ZMBE.

T/K	C_{inh}/g·L^{-1}	R_s/Ω·cm^2	Y_0/μΩ^{-1}·cm^{-2}·s^n	n	R_{ct}/Ω·cm^2	f_{max}/Hz	C_{dl}/μF·cm^{-2}	η_{EIS}/%	θ_{EIS}
298	0	1.3	117.1	0.862	49.5	56.84	52.0	–	–
	0.1	1.5	94.5	0.904	80.6	35.76	56.2	38.6	0.386
	0.5	1.5	97.3	0.868	129.9	22.31	50.7	61.9	0.619
	1.0	1.4	77.4	0.856	188.1	22.31	38.0	73.7	0.737
	3.0	1.4	83.8	0.836	207.1	22.31	37.3	76.1	0.761
	5.0	1.5	70.7	0.854	275.2	18.00	35.5	82.0	0.820
308	0	1.4	179.3	0.916	17.1	91.53	105.1	–	–
	0.1	1.3	138.7	0.909	35.2	56.84	81.2	51.4	0.514
	0.5	1.4	101.1	0.870	87.6	35.76	50.0	80.5	0.805
	1.0	1.3	103.8	0.852	103.5	28.27	48.2	83.5	0.835
	3.0	1.4	82.5	0.851	148.1	28.27	38.1	88.5	0.885
	5.0	1.2	101.3	0.832	171.4	22.31	44.2	90.0	0.900
318	0	1.3	247.5	0.932	8.1	144.97	155.7	–	–
	0.1	1.4	199.2	0.906	16.8	91.53	109.6	51.8	0.518
	0.5	1.3	158.2	0.866	41.7	56.84	72.0	80.6	0.806
	1.0	1.1	178.6	0.831	56.1	45.00	68.8	85.6	0.856
	3.0	1.2	124.3	0.833	87.5	35.76	50.3	90.7	0.907
	5.0	1.1	105.4	0.840	100.1	35.76	44.3	91.9	0.919

one time constant.

As indicated in Table 3, f_{max} decreases with increasing the ZMBE concentration, thus the frequency response time of the double electric layer capacitor is prolonged, and the values of Y_0 and C_{dl} decrease. According to the Helmholtz model (Hu et al., 2017b; Tang et al., 2023):

$$C = \frac{\varepsilon^0 \varepsilon S}{d} \tag{6}$$

the capacitance value (C) is related to the real surface area of the bipolar plates (S), the relative permittivity (ε), and the distance of the bipolar plates (d). ε of water molecules and active chloride ions generally is higher than that of other substances, but the molecular size of the former is generally smaller than that of organic components in ZMBE.

In the absence of ZMBE, water molecules and active chloride ions are adsorbed on the MS surface. The addition of ZMBE leads to the replacement of water molecules and chloride ions by active organic molecules, resulting in a decrease in ε and an increase in d. Since the adsorption of ZMBE has slight influence on n, the change in the actual surface area of the electric double-layer capacitance can be negligible. Therefore, the adsorption of ZMBE on the MS surface ultimately leads to a decrease in electric double-layer capacitance. In addition, when the protonated onium ions undergo electrostatic attraction with the initially adsorbed chloride anions, they are physically adsorbed on the MS surface, also contributing to a decrease in C_{dl}.

As indicated in Table 3, both η_{EIS} and θ_{EIS} exhibit an increase with solution temperature at the same ZMBE concentration. Specifically, at 298, 308, and 318 K, the maximum η_{EIS} of ZMBE is 82.0 %, 90.0 %, and 91.9 %, respectively. It is noteworthy that elevating the temperature of the HCl solution results in a serious decrease in R_{ct} and a severe increase in C_{dl}, indicating a reduction in the corrosion resistance of MS. The change patterns of η_{EIS} and η_{PDP} with ZMBE content and solution temperature are consistent, although the specific values differ. This discrepancy is attributed to the variances in testing principles and calculation methods between EIS diagrams and PDP curves.

4.4. *Comparison between ZMBE and other plant extracts*

Table 4 shows the comparison between ZMBE and other plant extracts as corrosion inhibitors for metals in 1 M HCl solution. On the whole, η of most plant extracts increases with the extract concentration and the medium temperature. But the optimal content and the maximum η of different plant extracts are distinct. Obviously, the active ingredients in various extracts are different and so are the functional groups and the electronic structures. In present work, η of ZMBE is greater than that of other compared plant extracts. It implies that ZMBE displays an excellent potential as an efficient, green, and renewable corrosion inhibitor for MS in HCl pickling solution.

4.5. *Adsorption behavior*

4.5.1. *Adsorption isotherms*

The adsorption behavior of organic molecules on the metal surface is an important criterion for assessing the effectiveness of corrosion inhibition (Huang et al., 2022). Electrochemical corrosion analysis shows that ZMBE exhibits an outstanding corrosion inhibition effect on MS in 1 M HCl solution and provides the corrosion inhibition mechanism of "geometric coverage" effect. θ is equal to η. The adsorption isotherm describes the relationship between coverage and concentration of the

Table 4
Comparison between ZMBE and other plant extracts as corrosion inhibitors for metals in 1 M HCl solution.

Plant extracts	Metals	Change of η with inhibitor content	Optimal content/g·L^{-1}	Maximum η	Reference
Moringa oleifera leaf	API 5L X52 steel	Increase	4.0	73 % at 298 K 90 % at 333 K	Didouh et al., 2023
Lilium brownii leaf	X70 steel	Increase	0.2	84.3 % at 298 K 85.2 % at 308 K	Zuo et al., 2020
Walnut fruit green husk	Mild steel	Increase	0.8	84.5 % at 298 K	Shahmoradi et al., 2021
Oestrus ovis larvae	Mild steel	First increase, then decrease	1.0	86.0 % at 301 K	Mobtaker et al., 2022
Ginkgo leaf	X70 steel	Increase	0.2	89.9 % at 298 K 92.5 % at 318 K	Qiang et al., 2018
Akebia trifoliate koiaz peel	Mild steel	Increase	0.8	90.0 % at 298 K	Zhang et al., 2021
Randia monantha benth	Mild steel	Increase	1.0	90.0 % at 298 K	Hernandez et al., 2023
Mangifera indica (mango) leaf	Mild steel	First increase, then decrease	0.8	92.0 % at 298 K	Ramezanzadeh et al., 2018
Pelargonium gravelons	Mild steel	Increase	0.2	92.6 % at 308 K	Boussalem et al., 2022
Tragacanth gum	Mild steel	Increase	0.6	92.7 % at 298 K	Mohammad et al., 2023
Prickly pear nopales pulp	XC38 steel	First increase, then decrease	0.25	93.2 % at 298 K	Madaci et al., 2023a
Oxalis corniculata L.	Carbon steel	Increase	0.5	93.7 % at 298 K	Wang et al., 2023
White turnip bark	Carbon steel	Increase	0.8	94.4 % at 298 K	Alemnezhad et al., 2023
Bee pollen	Copper	Increase	7.0	94.5 % at 298 K	Ahmed et al., 2020
Acanthopanax senticosus leaf	Carbon steel	Increase	0.15	94.5 % at 298 K	Liao et al., 2022
Cabbage	X70 steel	Increase	0.1	95.9 %	Sun et al., 2022
Zea mays bracts	Mild steel	Increase	5.0	87.7 % at 298 K 94.8 % at 308 K 96.2 % at 318 K	Present work

organic inhibitor at a constant temperature and is profit to understand the adsorption film on the metal surface. Based on θ_{PDP} and θ_{EIS}, the following different adsorption isotherm equations were tried.

Langmuir adsorption isotherm (Shadi et al., 2023; Xu at al., 2022b):

$$\frac{C_{inh}}{\theta}=\frac{1}{K_{ads}}+C_{inh} \tag{7}$$

El-Awady adsorption isotherm (Bhardwaj et al., 2021; Dehghani et al., 2019b):

$$\ln\frac{\theta}{1-\theta}=\ln K'+y\ln C_{inh} \tag{8}$$

Temkin adsorption isotherm (Vaszilcsin et al., 2023):

$$\theta=-\frac{1}{2\alpha}\ln C_{inh}-\frac{1}{2\alpha}\ln b \tag{9}$$

Where θ is the coverage of ZMBE on the MS surface, i.e. θ_{PDP} and θ_{EIS} in Tables 2 and 3. C_{inh} is the mass concentration of ZMBE (g·L^{-1}). K_{ads} is the adsorption equilibrium constant (L·g^{-1}), and it can be determined by the intercept in Langmuir isotherm. In El-Awady isotherm, K_{ads} can be derived by K', i.e.$K_{ads}=K'^{(1/y)}$. Where $1/y$ stands for the number of water molecules which are replaced by one organic molecule (Jyothi and Ravichandran, 2014). b is the Temkin isotherm constant. α means the interaction force between the organic molecules in the adsorption layer (Jyothi and Ravichandran, 2014). A negative α indicates a repulsive force, while a positive α suggests an attractive force.

The fitting results of various adsorption isotherms are presented in Figs. 13-15 and Tables 5 and 6. At three experimental temperatures (298, 308, and 318 K), the adsorption of ZMBE on the MS surface strictly adheres to the Langmuir isotherm. While the resemblance of the El-Awady isotherm is not as robust as that of the Langmuir isotherm, it still holds a certain degree of reliability. Clearly, the adsorption of ZMBE on the MS surface does not conform to the Temkin isotherm.

The Langmuir isotherm, being an ideal adsorption model, assumes that the adsorption molecules do not interact with each other on a uniform solid surface and eventually reach equilibrium. Therefore, the active molecules in ZMBE form a monolayer adsorption film on the MS surface without interaction forces. This alignment with EIS results, where only one single capacitive arc and one single time constant are displayed. It further confirms the surface observations derived from SEM.

K_{ads} reflects the adsorption capacity of organic molecules (Khadija et al., 2023). A higher K_{ads} indicates a stronger adsorption capability of the active molecules on the MS surface, showing a better corrosion inhibition effect. As depicted in Table 5, K_{ads} increases with solution temperature, and the strongest adsorption capacity of ZMBE is at 318 K, coinciding with the η result.

As depicted in Fig. 14 and Table 6, the linear correlation coefficient for the El-Awady isotherm is nearly close to 1, suggesting that the adsorption of the active molecules on the MS surface also follows the El-Awady model. All $1/y$ is greater than one, but it decreases with the increasing of solution temperature. A single organic molecule can displace multiple water molecules and occupy multiple active adsorption sites on the MS surface (Jyothi and Ravichandran, 2014).

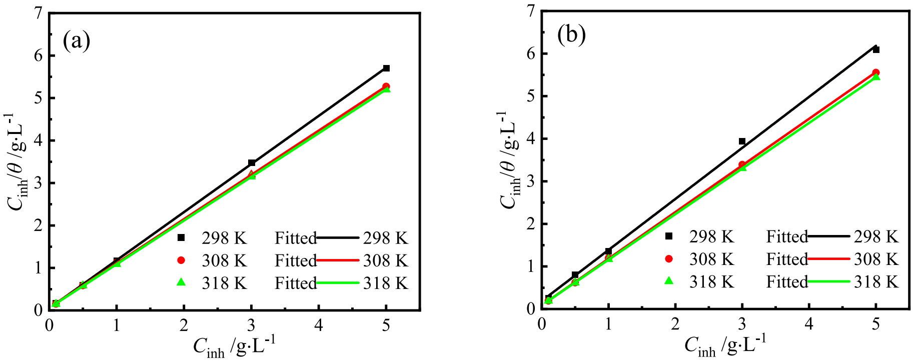

Fig. 13. Langmuir isotherms of ZMBE on the MS surface based on (a) PDP and (b) EIS results.

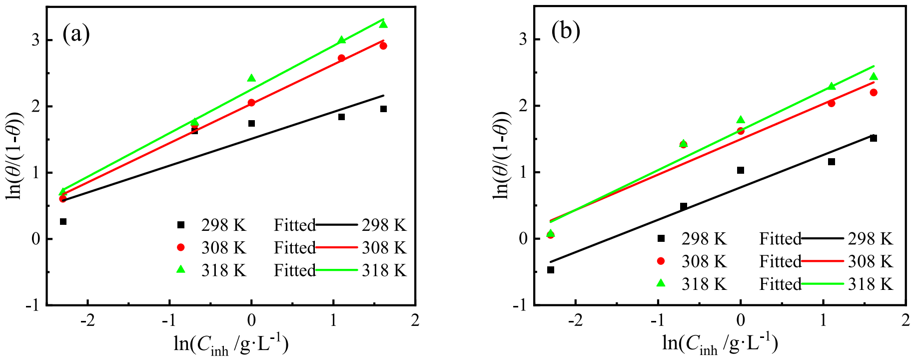

Fig. 14. El-Awady isotherms of ZMBE on the MS surface based on (a) PDP and (b) EIS results.

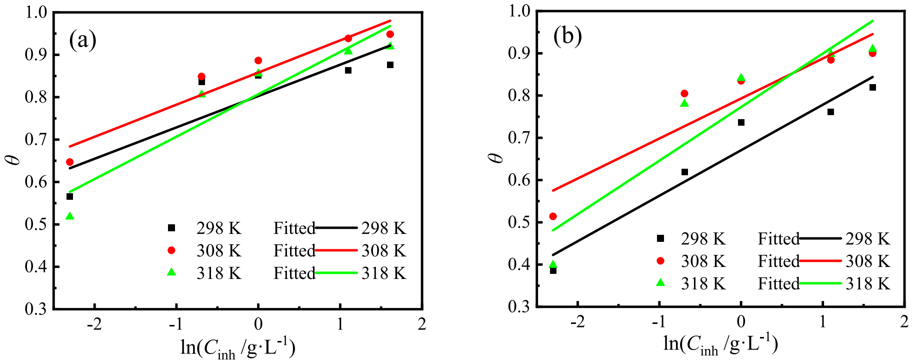

Fig. 15. Temkin isotherms of ZMBE on the MS surface based on (a) PDP and (b) EIS results.

Table 5
Fitting results for the Langmuir isotherms of ZMBE on the MS surface.

Test methods	T/ K	R^2	Slope	Intercept	K_{ads}/ L·g^{-1}	ΔG_{ads}/ kJ·mol^{-1}
PDP	298	0.999	1.13	0.0633	15.8	−23.9
	308	0.999	1.04	0.0614	16.2	−24.7
	318	0.999	1.03	0.0603	16.6	−25.6
EIS	298	0.998	1.20	0.1726	5.8	−21.4
	308	0.999	1.10	0.0899	11.1	−23.8
	318	0.999	1.07	0.0872	11.5	−24.6

However, the number of active adsorption points that can be replaced by organic molecules tends to decrease at higher temperature. This may be linked to the alterations in the adsorption mode, such as the relative ratios of physical adsorption to chemical adsorption (Li et al., 2021b; Luo et al., 2023). Furthermore, the variation of K_{ads} with temperature is consistent based on both the El-Awady and Langmuir isotherms. The optimal adsorption ability of organic molecules is observed at 318 K, followed by 308 K.

4.5.2. Adsorption thermodynamic parameters

To further investigate the adsorption behavior of ZMBE on the MS surface, the adsorption Gibbs free energy (ΔG_{ads}) was calculated by K_{ads} (Martinez-Gonzalez et al., 2023):

$$K_{ads} = \frac{1}{\rho_{solvent}} \exp\left(-\frac{\Delta G_{ads}}{RT}\right) \quad (10)$$

Where R is the gas constant, 8.314 J•K^{-1}•mol^{-1}; T is the thermodynamic temperature (K); $\rho_{solvent}$ is the mass concentration of the solvent (i.e. water) in the corrosion system (g·L^{-1}). The concentration of ZMBE is relatively low and can be neglected. Thus, $\rho_{solvent}$ of 1 M HCl solution is about 962 g·L^{-1}.

A negative ΔG_{ads} indicates a spontaneous adsorption process of organic molecules on the metal surface. On the contrary, it is the desorption process (Mehdi et al., 2019; Nesane et al., 2023). Generally, when ΔG_{ads} is greater than −20 kJ•mol^{-1}, it is physical adsorption. When ΔG_{ads} is less than −40 kJ•mol^{-1}, it is chemical adsorption. And it is mixed adsorption when ΔG_{ads} ranges from −40 to −20 kJ•mol^{-1} (Mehdi et al., 2019; Obi-Egbedi et al., 2012). As shown in Tables 5 and 6, all ΔG_{ads} is negative, and it ranges from −40 to −20 kJ•mol^{-1}, closer to −20 kJ•mol^{-1}. The adsorption process of active molecules on the MS

Table 6
Fitting results for the El-Awady isotherms of ZMBE on the MS surface.

Test methods	T/K	R^2	Slope	Intercept	1/y	K'	K_{ads}/L·g^{-1}	ΔG_{ads}/kJ·mol^{-1}
PDP	298	0.847	0.41	1.4115	2.4	4.1	31.2	−25.6
	308	0.991	0.59	2.0391	1.7	7.7	31.4	−26.4
	318	0.988	0.65	2.2752	1.5	9.7	33.0	−27.4
EIS	298	0.941	0.46	0.7731	2.2	2.5	5.4	−21.2
	308	0.921	0.53	1.4364	1.9	4.2	14.9	−24.5
	318	0.953	0.60	1.6316	1.7	5.1	15.2	−25.4

surface is spontaneous, and it is a mixed adsorption mainly based on physical adsorption. ΔG_{ads} is more negative with a higher temperature, so the proportion of chemical adsorption in mixed adsorption is enhanced.

4.5.3. Adsorption kinetic parameters

The corrosion rate of MS (v) was approximately calculated based on Faraday's law:

$$v = \frac{Mi_{corr}}{nF} \tag{11}$$

Where M is the relative atomic mass of MS, about 56 g·mol^{-1}. n is the number of exchanged charges in the oxidation reaction of Fe, taken as 2. F is the Faraday constant, nearly 26.8 A·h. According to the Arrhenius and transition state theories (Mrani et al., 2023), the effect of ZMBE on kinetic parameters of the corrosion reaction of MS in 1 M HCl solution was analyzed.

Arrhenius equation (Chaudhary et al., 2012a, 2013b, 2016c):

$$\ln v = \ln A - \frac{E_a}{RT} \tag{12}$$

Transition state equation (Lin et al., 2021a):

$$\ln\left(\frac{v}{T}\right) = -\frac{\Delta H_a}{RT} + \frac{\Delta S_a}{R} + \ln\left(\frac{R}{Nh}\right) \tag{13}$$

Where A is the pre-exponential factor in the Arrhenius equation. E_a is the activation energy of the corrosion reaction of MS. R and T are similar to those in Eq. (11). N is the Avogadro's constant, 6.02×10^{23} mol^{-1}. h is the Planck's constant, 6.626×10^{-34} J·s^{-1}. ΔH_a and ΔS_a are the activation enthalpy and activation entropy of the corrosion reaction of MS.

Fig. 16 shows the fitting results of the Arrhenius and Transition state kinetic equations for the corrosion reaction of MS in 1 M HCl solution with different ZMBE concentration. Table 7 lists the corresponding parameters of the activation reaction. Both kinetic equations for the corrosion reaction of MS exhibit a good linear relationship.

A significant decrease in E_a is a characteristic of the chemical adsorption, while a remarkable increase in E_a indicates the physical adsorption (Lin et al., 2024c; Abdullah et al., 2023). As shown in Table 7, the addition of ZMBE results in a decrease in E_a. Specifically, E_a is 69.2 kJ·mol^{-1} in the absence of ZMBE, and it decreases to 22.9 kJ·mol^{-1} in the presence of 5.0 g·L^{-1} ZMBE. The slight decrease in E_a can be attributed to the mixed adsorption of active ingredients in ZMBE on the MS surface. Obviously, the physical and chemical adsorption abilities of various organic molecules in ZMBE are different. As the temperature increases, the physical adsorption will be weakened, and so is their inhibitory effect. Meanwhile, the irreversible chemical adsorption caused by electron sharing requires higher concentration of ZMBE.

The pre-exponential factor A reflects the quantity of active sites available for the corrosion reaction of the metal (Garai et al., 2012). Upon the addition of ZMBE to the HCl solution, A undergoes a significant decrease. Specifically, it is 6.59×10^{13} g·m^{-2}·h^{-1} in the blank solution, and it diminishes to 5.65×10^{5} g·m^{-2}·h^{-1} in the presence of 5.0 g·L^{-1} ZMBE, reducing by more than eight orders of magnitude. This substantial reduction in A is clearly attributed to the adsorption of organic molecules on the micro-anodes and micro-cathodes of the MS surface. The adsorption film inhibits both the anodic and cathodic corrosion reactions, which has been confirmed by the PDP and EIS tests. As the concentration of ZMBE increases, the adsorption of organic molecules intensifies, and more active sites on the MS surface are covered. The variation of A with ZMBE concentration provides further confirmation of the inhibition mechanism of the "geometric coverage" effect.

Table 7
Effect of ZMBE concentration on kinetic parameters of corrosion reaction of MS in 1 M HCl solution.

C_{inh}/g·L^{-1}	A/g·m^{-2}·h^{-1}	E_a/kJ·mol^{-1}	ΔH_a/kJ·mol^{-1}	ΔS_a/J·mol^{-1} K^{-1}
0	6.59×10^{13}	69.2	66.6	−3.1
0.1	2.09×10^{12}	62.8	56.0	−31.9
0.5	9.60×10^{10}	57.1	54.5	−43.3
1.0	7.74×10^{8}	41.9	43.2	−83.3
3.0	3.89×10^{6}	27.4	24.8	−146.5
5.0	5.65×10^{5}	22.9	20.3	−165.2

As depicted in Table 7, ΔS_a is reduced obviously after ZMBE is added, implying a significant improvement in orderliness of the MS surface. This can be attributed to the ordered arrangement and adsorption of the active components, which replaces the initially disordered adsorption of chloride ions and water molecules (Du et al., 2022b). With an increase in ZMBE concentration, ΔS_a becomes more negative, and a higher order of the MS surface is obtained. Furthermore, ΔH_a at all experimental conditions is positive, suggesting an endothermic process of the corrosion reaction of MS. Consequently, with an elevation in the temperature of the HCl solution, the corrosion rate of MS significantly increases. But the endothermic effect decreases with an increase in ZMBE concentration, leading to a reduction in the corrosion rate.

4.6. Theoretical simulation results

4.6.1. DFT calculations

To investigate the adsorption behavior of the active ingredients on the MS surface and to further confirm their corrosion inhibition mechanism of "geometric coverage" effect, DFT calculations were conducted. The distribution of the front molecular orbitals of the active molecules was studied. And the relevant activity energy parameters were calculated, which included the highest occupied molecular orbital energy level (E_{HOMO}), the lowest unoccupied molecular orbital energy level (E_{LUMO}), the energy gap (ΔE) reflecting the molecular stability and reactivity, the ionization potential (I) representing how easily a molecule can be ionized (Aihara, 1999; Yoshidaa and Aihara, 1998), the

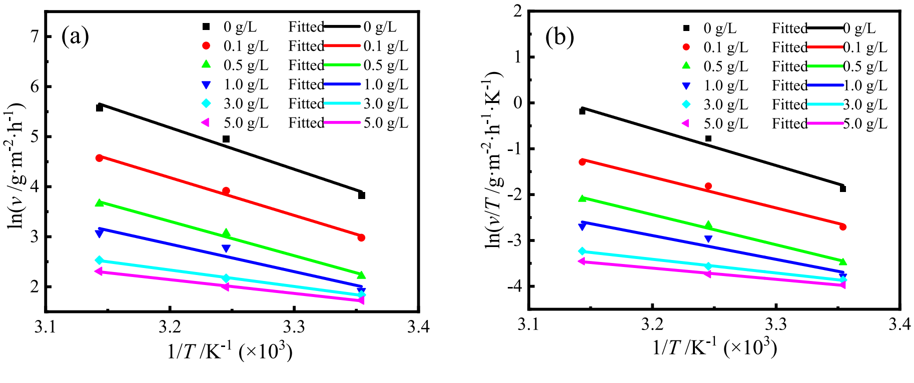

Fig. 16. Fitting lines of the kinetics equations for corrosion reaction of MS in 1 M HCl solution with different content of ZMBE: (a) Arrhenius, and (b) Transition state.

electron affinity (A) describing the released energy when a molecule acquires an electron, the electronegativity (χ), the global hardness (ζ), and the electron transfer capability (ΔN) reflecting the ability of organic molecules sharing electrons with metal atoms (Nabajyoti et al., 2019). The calculation formulas are as follows (Wang et al., 2023c; Wu et al., 2023b):

$$\Delta E = E_{\text{LUMO}} - E_{\text{HOMO}} \tag{14}$$

$$I = -E_{\text{HOMO}} \tag{15}$$

$$A = -E_{\text{LUMO}} \tag{16}$$

$$\chi = \frac{I + A}{2} = -\frac{E_{\text{LUMO}} + E_{\text{HOMO}}}{2} \tag{17}$$

$$\zeta = \frac{I - A}{2} = \frac{E_{\text{LUMO}} - E_{\text{HOMO}}}{2} \tag{18}$$

$$\Delta N = \frac{\phi_{\text{Fe}} - \chi_{\text{inh}}}{2(\zeta_{\text{Fe}} + \zeta_{\text{inh}})} \tag{19}$$

Where χ_{inh} and ζ_{inh} are the electronegativity and global hardness of organic molecules (Bahlakeh et al., 2017; Madaci et al., 2023b). ζ_{Fe} is the global hardness of Fe, which can be neglected (Haldhar et al., 2021; Madaci et al., 2023b). ϕ_{Fe} is the work function of Fe, about 4.82 eV (Savaş et al., 2023; Sukdeb et al., 2023). The work function is the minimum energy required to move an electron from the interior to the surface of a solid. The electronegativity does not consider the interaction between electrons, but it only considers the Fermi energy of free electron gas. Therefore, the electronegativity of Fe (χ_{Fe}) is replaced by ϕ_{Fe} during calculating ΔN, as shown in Eq. (19).

The electron-rich sites in organic molecules, such as heteroatoms O and N, multiple bonds, aromatic rings, contain lone-pair and/or π electrons which can be provided to the unfilled 3*d* orbitals of Fe (Madaci et al., 2023b). In a similar manner, the lone-pair electrons in organic molecules act as electron acceptors, receiving electrons from the filled 3*d* orbitals of Fe. This electron sharing and the coordination bonds formed between organic molecules and Fe atoms contribute to the chemical adsorption process (Sirsendu et al., 2021; Wang et al., 2023c). Organic compounds are consequently adsorbed on the MS surface, forming a protective film to impede the contact of the corrosive medium with the metal. The site centers in organic molecules play a predominant role in governing the binding between organic molecules and metal atoms through the interactions of electron donor and electron acceptor (El-Mokadem et al., 2023; Lgaz and Lee, 2023). Based on the DFT calculations, the impact of protonation of various heteroatoms in active ingredients on the molecular geometric equilibrium configuration was analyzed. The optimal protonation atom and the corresponding equilibrium configuration were identified, as shown in Fig. 17.

Fig. 18 shows the distributions of HOMO and LUMO for active ingredients of hydroxycinnamic acid, dimboa, glucuronic acid, and rutin under the neutral state. In the case of neutral hydroxycinnamic acid, the HOMO and LUMO distributions are spread across the entire molecular configuration, encompassing the benzene ring, hydroxyl, carboxyl, and double bonds. Similarly, for neutral dimboa, HOMO and LUMO are also distributed across the whole molecule, including two aromatic rings, two hydroxyls, and one carbonyl. These regions are rich in π electrons and/or lone-pair electrons, enabling both neutral hydroxycinnamic acid and dimboa to donate and accept electrons from Fe atoms. The synergistic adsorption effect involves electron donation and acceptance, facilitating electron-sharing coordination with Fe atoms on the MS surface. For neutral glucuronic acid, the distributions of HOMO and LUMO are slightly smaller. HOMO primarily concentrates on carbonyl and its adjacent two hydroxyls, while LUMO is mainly distributed on carbonyl and its adjacent four hydroxyls. In the case of neutral rutin, HOMO and LUMO are predominantly centered on benzene ring 1, aromatic ring 2, and benzene ring 3, as well as on hydroxyls attached to benzene rings 1 and 3 and carbonyl attached to aromatic ring 2. These aromatic rings, hydroxyls, and carbonyls are capable of receiving electrons from Fe ions, forming stable chelates and producing chemical adsorption effect. Due to the relatively large spatial distortion structure of neutral rutin molecules, they exhibit greater directionality in the binding process with the surface (Rachid et al., 2022).

Fig. 19 shows the distributions of HOMO and LUMO for the protonated active ingredients in ZMBE. Notably, protonation has little impact on HOMO and LUMO of hydroxycinnamic acid and dimboa. It suggests that hydroxycinnamic acid and dimboa, in both neutral and

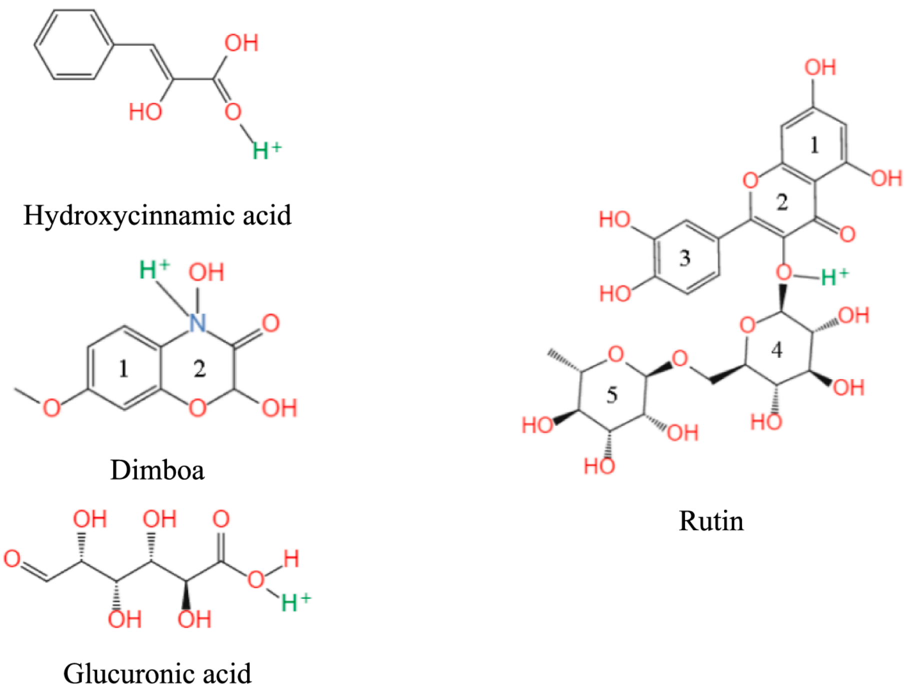

Fig. 17. Geometric equilibrium configurations of the optimal protonated components in ZMBE.

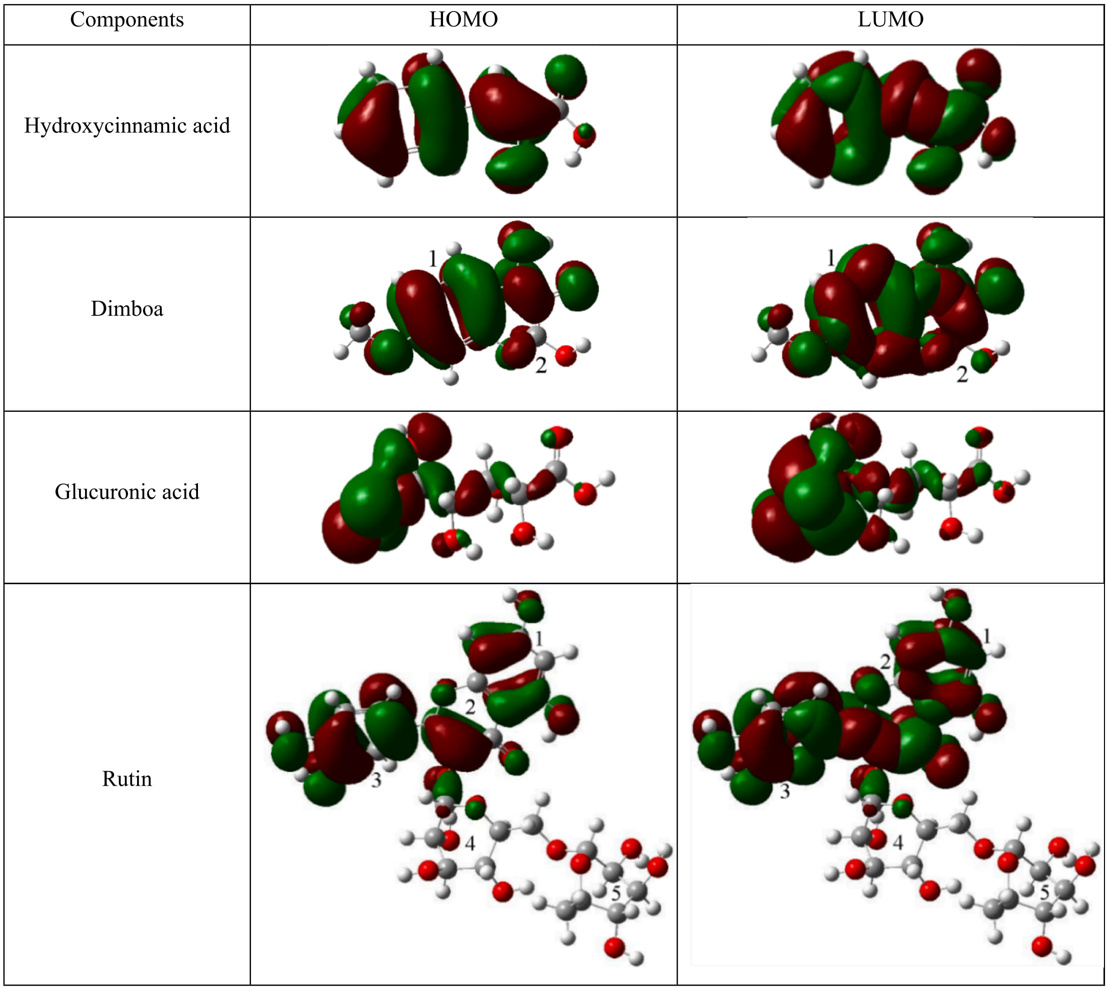

Fig. 18. Frontier molecular orbital distributions of typical active ingredients in ZMBE at the neutral state.

protonated states, retain the ability of electron donation and acceptance. In addition, the protonated hydroxyls in hydroxycinnamic acid and dimboa carry a positive charge, establishing electrostatic attraction with the negatively charged chloride ions initially adsorbed on the MS surface, leading to physical adsorption on the MS surface. Moreover, the polar functional groups in hydroxycinnamic acid and dimboa can also undergo physical adsorption through dispersion forces, induction effects, and other mechanisms. Consequently, hydroxycinnamic acid and dimboa experience both chemical and physical adsorption through the synergistic effect of multiple channels. The protonation of glucuronic acid has a slight impact on its electron-donating ability, but it enhances electron-accepting capability.

This results in a strengthened synergistic adsorption effect for glucuronic acid after protonation. Given its more favorable protonation in an acidic environment, glucuronic acid provides an improved corrosion protection for MS. However, under neutral and alkaline conditions, the protonation of glucuronic acid is limited, which will affect its corrosion inhibition function. For rutin, the HOMO distribution remains largely unaffected by protonation, while the LUMO distribution is slightly weakened on aromatic rings 1 and 2 and enhanced on heterocycle 4. This variation may be attributed to the spatial distortion inherent in the large molecule of rutin (Qiang et al., 2018).

Table 8 presents the reaction activity energy parameters of typical ingredients in ZMBE. A larger E_{HOMO} implies a stronger electron-donating ability of the organic molecule, while a smaller E_{LUMO} indicates a stronger capability to accept electrons. In the neutral state, there is no significant difference in E_{HOMO} among the four active ingredients, with dimboa and rutin having slightly higher E_{HOMO} values. The variation in E_{LUMO} among four ingredients is smaller than 1 eV, with rutin and hydroxycinnamic acid exhibiting slightly lower E_{LUMO} values. After protonation, the decrease in E_{LUMO} is more pronounced than that in E_{HOMO}. The reduction in all E_{HOMO} values is less than 1 eV, while E_{LUMO} of hydroxycinnamic acid, dimboa, glucuronic acid, and rutin is reduced by about 1.53, 3.40, 2.40, and 0.35 eV, respectively. The changes in E_{HOMO} and E_{LUMO} suggest that the protonation of active ingredients weakens their electron-donating ability, but it significantly enhances their electron-accepting ability, with the exception of rutin. In the protonated state, E_{HOMO} for hydroxycinnamic acid, dimboa, and rutin is similar, and E_{LUMO} for hydroxycinnamic acid, dimboa, and glucuronic acid is comparable. In both neutral and protonated states, the mechanism through which the active ingredients share electrons with Fe atoms and form coordination bonds is altered to some extent. However, they ultimately result in the formation of the coordination compounds by the synergistic effect of chemical adsorption and physical adsorption, effectively blocking the contact between MS and the solution and suppressing the corrosion reaction.

ΔE serves as an indicator of electron stability and chemical reactivity for organic molecules (El-Faydy et al., 2022; Prasad et al., 2022b). A smaller ΔE suggests a greater activity of organic molecules, a higher propensity for electron sharing with Fe atoms, and a stronger interaction with the MS surface. As shown in Table 8, ΔE for neutral hydroxycinnamic acid and rutin is relatively smaller than that of dimboa and glucuronic acid, primarily attributed to the smaller E_{LUMO} of the former two. After protonation, all ΔE for the four ingredients decreases. While

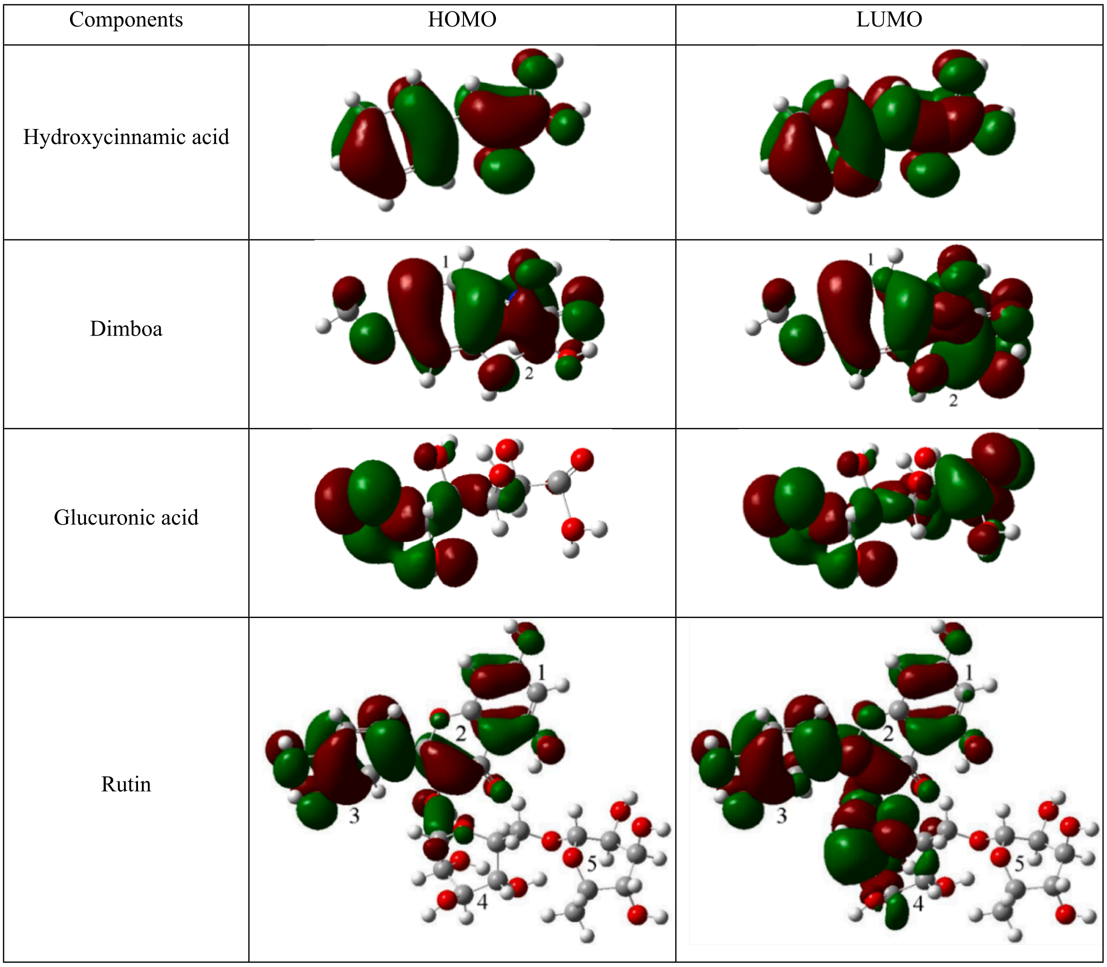

Fig. 19. Frontier molecular orbital distributions of the typical active ingredients in ZMBE in the protonated state.

Table 8
Reactivity energy parameters of active ingredients in ZMBE.

Components	E_{HOMO}/eV	E_{LUMO}/eV	ΔE/eV	I/eV	A/eV	ζ/eV	χ/eV	ΔN/eV	μ/D
Neutral state									
Hydroxycinnamic acid	−6.47	−1.98	4.49	6.47	1.98	2.24	4.22	0.13	7.02
Dimboa	−5.94	−1.00	4.93	5.94	1.00	2.47	3.47	0.27	6.28
Glucuronic acid	−7.11	−1.24	5.86	7.11	1.24	2.93	4.18	0.11	5.40
Rutin	−6.12	−2.00	4.12	6.12	2.00	2.06	4.06	0.18	10.14
Protonated state									
Hydroxycinnamic acid	−6.93	−3.51	3.42	6.93	3.51	1.71	5.22	−0.12	12.97
Dimboa	−6.47	−4.40	2.01	6.47	4.40	1.04	5.54	−0.30	4.78
Glucuronic acid	−8.08	−3.64	4.44	8.08	3.64	2.21	5.86	−0.23	9.29
Rutin	−6.38	−2.35	4.03	6.38	2.35	2.01	4.37	0.11	16.19

the decrease in rutin is relatively small, dimboa exhibits the most significant reduction (about −2.92 eV), owing to the substantial decrease in E_{LUMO} (near −3.40 eV). Except rutin, the reactivity of the other three ingredients significantly increases after protonation. In neutral and alkaline environments, protonation of organic molecules is difficult, and the protonated molecules might not exist. For rutin, its chemical reactivity is almost unaffected by its states. Therefore, the electron sharing and the formation of the adsorption film of rutin is less susceptible to the pH of the solution. Rutin is likely to exhibit excellent corrosion inhibition properties in neutral and alkaline media. This is distinguished from hydroxycinnamic acid, dimboa, and glucuronic acid which may provide effective corrosion inhibition primarily in acidic conditions.

ΔN reflects the electron transfer ability of organic molecules to metal atoms (Kellal et al., 2023; Kumar et al., 2022). When ΔN is smaller than 3.6 eV, a larger ΔN indicates a higher reactivity and a stronger electron-donating capability of organic molecules. A positive ΔN implies that the organic molecules primarily act as the electron donors to metal atoms. Conversely, a negative ΔN indicates that the organic molecules tend to receive electrons from metal atoms (Singha et al., 2017; Swathi et al., 2023). In both neutral and protonated states, ΔN of four ingredients is positive, with dimboa and rutin exhibiting the highest ΔN. After protonation, dimboa, glucuronic acid and hydroxycinnamic acid tend to receive electrons, and dimboa has the most significant change. ΔN of rutin is the least variable. This further confirms that the electron-donating and electron-accepting ability of rutin is almost unaffected by protonation.

According to the maximum hardness principle, there is a correlation between chemical reactivity and ζ (Kaya and Kaya, 2015). A larger ζ implies a greater chemical stability of the chelates, an enhancement of the charge transfer resistance, and a stronger corrosion inhibition capability (Hu et al., 2016c). As indicated in Table 8, the stability of the complexes formed by neutral molecules with Fe ions is high, but it overall decreases after protonation. Rutin is a special case in which the stability of the corresponding chelates remains almost unchanged.

χ serves as an indicator of the electron-attracting ability of organic molecules (Mrani et al., 2023; Rahma et al., 2023; Wang et al., 2022d). A larger χ indicates that the formed chemical bonds are less stable, which are unfavorable for the protection of the metal surface. μ is related to the polarity of organic molecules (Bayram et al., 2018; Mustafa et al., 2019; Wang et al., 2022d). Generally, a higher μ corresponds to a stronger intermolecular interaction, which favors the adsorption of organic molecules on the metal surface through electron forces and provides a better corrosion inhibition (Ech-Chebab et al., 2022; Zhang et al., 2023b). As shown in Table 8, at both neutral and protonation states, rutin exhibits the highest μ, suggesting the most significant corrosion inhibition effect on MS.

4.6.2. MD calculations

MD simulations were conducted to further understand the interaction between organic molecules and the MS surface and to clarify the corrosion inhibition and adsorption mechanisms. The adsorption energy (E_{ads}) was calculated (Hou et al., 2021; Tan et al., 2024a):

$$E_{\text{ads}} = E_{\text{tot}} - (E_{\text{met+sol}} + E_{\text{inh}}) \tag{20}$$

Where E_{tot} is the total energy of the entire simulation system, including water molecules, organic molecules, and Fe atoms. $E_{\text{met+tot}}$ is the energy of the simulation system merely with water molecules and Fe atoms. E_{inh} is the energy of the simulation system only with organic molecules.

Fig. 20 and 21 present the snapshots of the side and top views of the final equilibrium configurations of four active ingredients on the Fe (1 1 0) plane. In both neutral and protonated states, hydroxycinnamic acid and dimboa are adsorbed in a fully parallel manner, aligning with the results of HOMO and LUMO which distribute on the entire molecular configurations. In the case of neutral glucuronic acid, apart from one hydroxyl and one C–C bond, the rest are adsorbed parallel to the Fe (1 1 0) plane, different from the results of HOMO and LUMO distributions. It can be attributed to the chelation reactions between carboxyl and Fe ions, along with the physical adsorption caused by the dispersion and induction forces between the polar hydroxyls and the Fe(1 1 0) surface (Tan et al., 2023b). For protonated glucuronic acid, the entire molecule is adsorbed parallel to the Fe(1 1 0) surface, resembling LUMO distribution but differing from HOMO distribution. Therefore, the

Components	Neutral state	Protonated state
Hydroxycinnamic acid	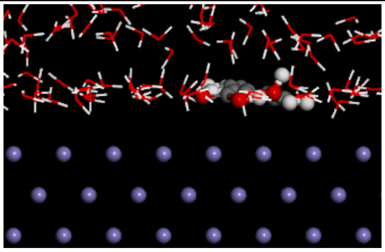	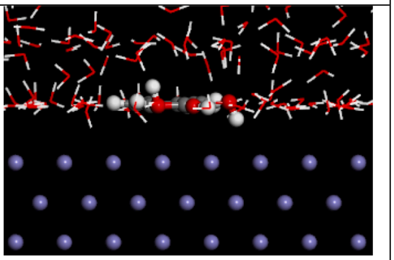
Dimboa	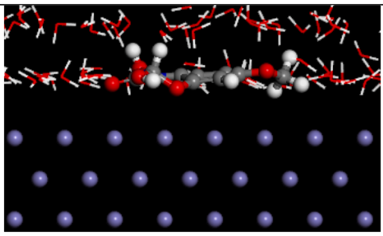	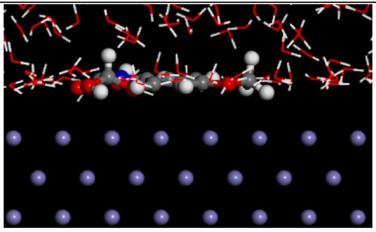
Glucuronic acid	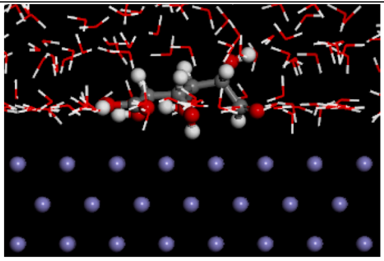	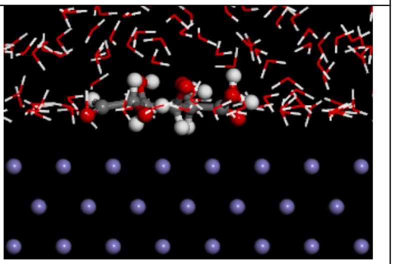
Rutin	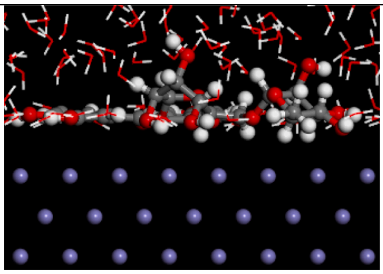	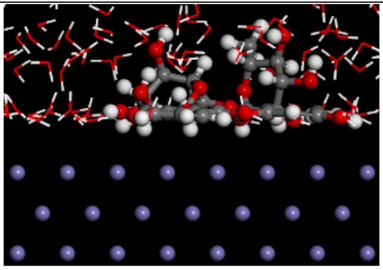

Fig. 20. Snapshot of side view of final equilibrium configurations of the active ingredients on the Fe(1 1 0) plane.

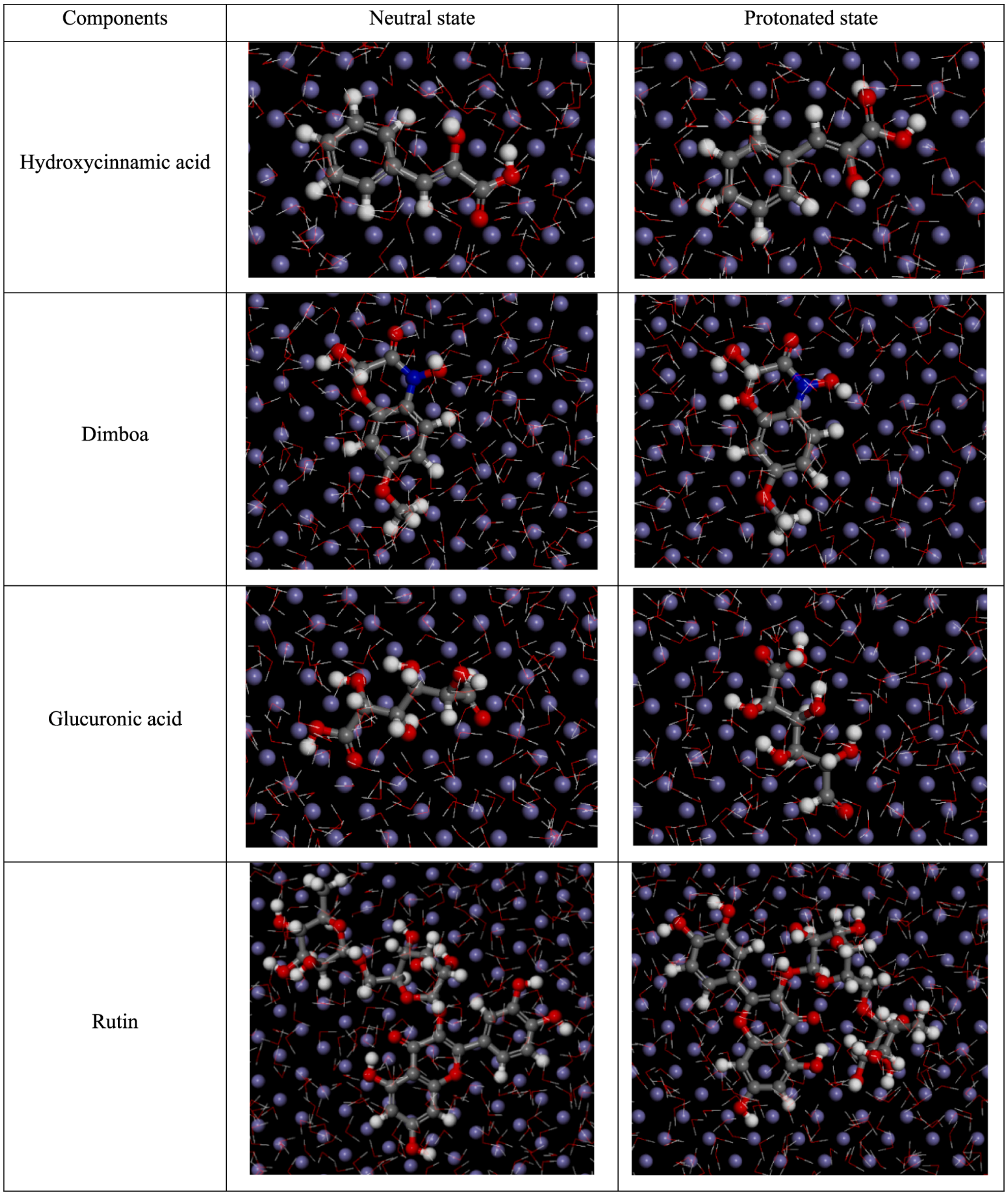

Fig. 21. Snapshot of top view of final equilibrium configurations of the active ingredients on the Fe(1 1 0) plane.

protonated glucuronic acid undergoes both physical and chemical adsorption, as described above.

The positively charged protonated oxygen atom in carboxyl creates electrostatic attraction with the negatively charged chloride ions initially adsorbed on the Fe(1 1 0) surface, further promoting the physical adsorption. For neutral rutin, benzene rings 1 and 3, along with three heterocycles, are adsorbed parallel to the Fe(1 1 0) plane, while some hydroxyls deviate, corresponding to the DFT results. In the case of protonated rutin, benzene rings 1 and 3 are still adsorbed parallel to the Fe(1 1 0) surface, while heterocycles 4 and 5 are lifted off. This may be attributed to the distortion of the rutin molecule, where heterocycle 4 and benzene 3 have a smaller bond angle in their spatial distribution, making them more compact and mutually exclusive when receiving electrons (Dutta et al., 2017).

Table 9 shows E_{ads} of the active ingredients on the Fe(1 1 0) plane. All E_{ads} is negative, indicating a spontaneous adsorption process of the active molecules on the most stable Fe(1 1 0) plane. A lower E_{ads} value indicates a stronger adsorption performance (Berrissoul et al., 2021b). E_{ads} of rutin is 329.8 eV in the neutral state, and it is 375.6 eV in the protonated state, obviously smaller than that of glucuronic acid, hydroxycinnamic acid, and dimboa. This difference can be attributed to the number of aromatic rings in the molecules. Glucuronic acid lacks benzene ring, hydroxycinnamic acid has one aromatic ring, dimboa has two aromatic rings, while rutin contains five aromatic rings. The aromatic rings directly influence the adsorption capability and the corrosion inhibition performance of the organic molecules (Lin et al., 2023b; Sergio et al., 2010).

Table 9

E_{ads} of the active ingredients in ZMBE on the Fe(1 1 0) plane (kcal·mol^{-1}).

Components	Neutral state	Protonated state
Hydroxycinnamic acid	−118.4	−136.4
Dimboa	−146.5	−183.5
Glucuronic acid	−126.8	−142.2
Rutin	−329.8	−375.6

4.7. Adsorption and corrosion inhibition mechanism

In an acidic corrosion system, the corrosion inhibition performance of organic molecules on metal primarily depends on their adsorption capacity, which is closely related to the molecular structure (Abdelaziz et al., 2021; Li et al., 2022c; Prasad et al., 2022b). There are two main types of adsorption patterns, i.e. physical adsorption and chemical adsorption. Physical adsorption is typically achieved through electrostatic attraction between charged metal surfaces and charged organic substances (Du et al., 2023a; Haldhar et al., 2021; Shahmoradi et al., 2022). It can also be facilitated through dispersion and induction forces related to the polar functional groups in organic molecules (Umoren et al., 2022; Xu et al., 2024a). On the other hand, chemical adsorption involves electron transfer, exchange, and/or sharing between the organic molecules and the metal atoms, resulting in the formation of coordination bonds and compounds. Chelation reactions between organic molecules and metal ions also contribute to the chemical adsorption (Madaci et al., 2023b; Sun et al., 2023c). To further elucidate the relationship between adsorption and corrosion inhibition mechanism of the active ingredients for MS, a corresponding model was constructed, as shown in Fig. 22.

The FT-IR, UV–visible and XPS analyses show that the organic molecules in ZMBE could interact with the MS surface to form an adsorption film. The DFT and MD results reveal that the adsorption behavior of organic molecules on the MS surface is linked to the distributions of HOMO and LUMO, as well as the quantity of π and lone-pair electrons. These characteristics, in turn, depend on the number of aromatic rings, heteroatoms, carbonyls, hydroxyls, double bonds, etc. Furthermore, these active centers in ZMBE determine the chemical reactivity of the organic molecules with Fe atoms/ions. As depicted in Fig. 22a, in the absence of ZMBE, the MS surface is covered by water molecules, hydrogen ions, and chloride ions, generating corrosion pits. After ZMBE was added (rutin was taken as an example), the organic molecules undergo a synergistic effect of physical and chemical adsorption through multiple factors, resulting in the mixed adsorption on the MS surface.

Based on the results of the Langmuir and El-Awady adsorption isotherms, the active molecules replace the initially adsorbed water molecules and chloride ions, forming a monolayer adsorption film. This closely fits the MD results where the active molecules adsorb flatly on the metal surface. The film blocks the mechanical contact between the corrosive medium and the metal surface, expelling the hydrogen ions and chloride ions. As a result, the active sites on the metal surface are

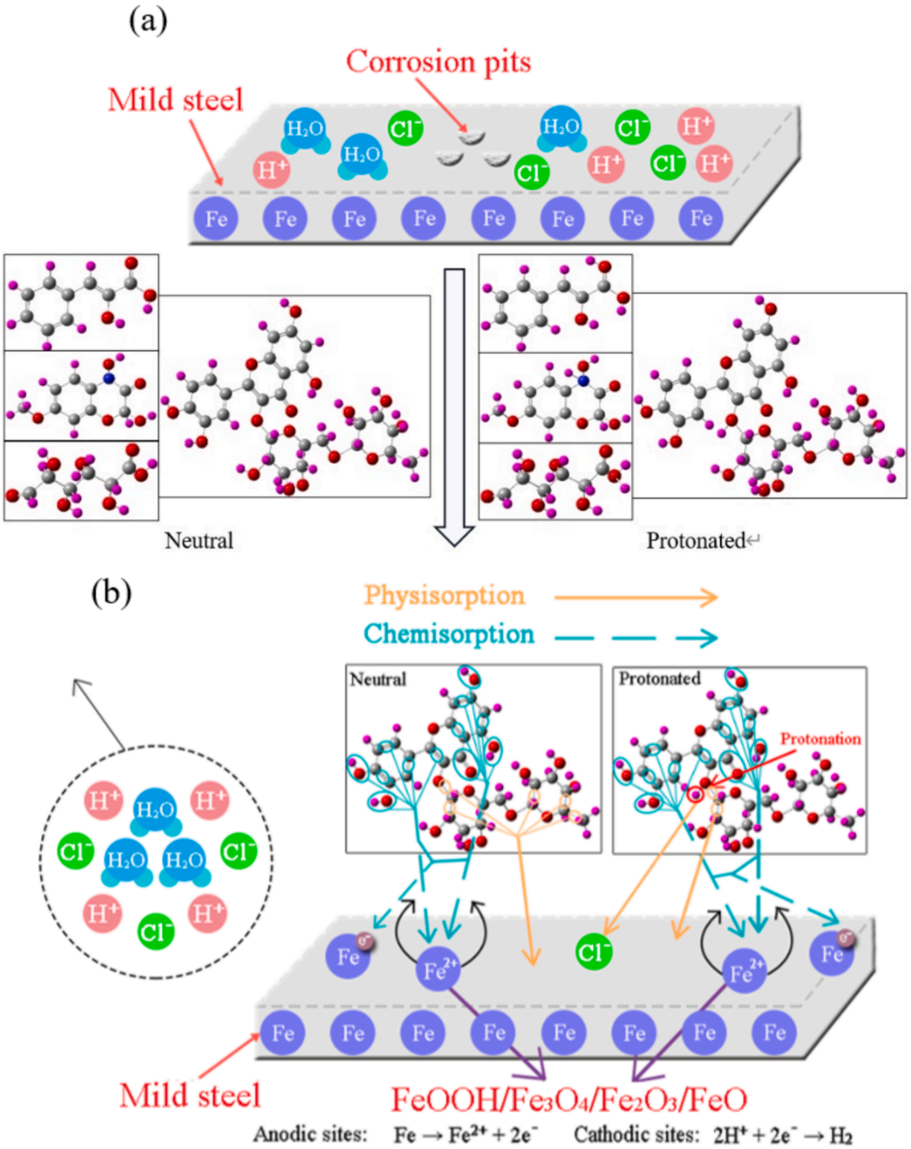

Fig. 22. Diagrammatic sketches for adsorption and corrosion inhibition mechanism of the active ingredients on MS.

reduced, inhibiting corrosion. This inhibition effect is primarily attributed to the rich content of aromatic rings, heteroatoms, carbonyls, hydroxyls, and other polar functional groups in ZMBE. These polar groups enable both physical and/or chemical adsorption. Hydroxycinnamic acid, dimboa, glucuronic acid, and rutin contain the mentioned functional groups. Rutin, with the most aromatic rings, exhibits excellent mixed adsorption effect and high coverage of the adsorption film. Although glucuronic acid lacks aromatic ring, its strongly polar carbonyl and hydroxyl groups also ensure the strong physical and chemical adsorption. It is worth noting that Fe^{2+} in the vicinity of the micro-anode covered by ZMBE can undergo further oxidation to Fe^{3+}. With the release of H^{+}, the pH near the micro-anode increases, promoting the deposition of iron (3 +) hydroxides and oxides and enhancing the corrosion resistance (Jian et al., 2023; Lin et al., 2024c; Zhao et al., 2023). In summary, ZMBE proves to be an outstanding corrosion inhibitor for MS in 1 M HCl pickling solution, with η up to 96.2 %, and the corrosion inhibition mechanism can be attributed to the “geometric coverage” effect.

5. Conclusions

The abundantly agricultural byproducts, *Zea mays* bracts, were utilized as a renewable source for green corrosion inhibitor, and *Zea mays* bracts extract (ZMBE) was obtained with extraction solvent of ethanol–water. ZMBE was applied as corrosion inhibitor for mild steel (MS) in 1 M HCl pickling solution. The corrosion inhibition and adsorption mechanism of ZMBE was investigated through experimental and theoretical calculations. The main conclusions are as follows.

1. ZMBE contains various phytochemicals such as carbohydrates, phenolic compounds, phenylpropanoids, and flavonoids. They are rich in organic functional groups like hydroxyls, carbonyls, carboxyls, aromatic rings, and heterocycles. These groups can form coordination bonds and complexes with Fe and adsorb on the MS surface.
2. ZMBE functions as a mixed-type corrosion inhibitor with a minor predominant inhibition of cathodic corrosion. ZMBE demonstrates an excellent corrosion inhibition behavior. At 298, 308, and 318 K, the maximum inhibition efficiency at 5.0 $g\cdot L^{-1}$ ZMBE is 87.7 %, 94.8 %, and 96.2 %, respectively.
3. The corrosion inhibition mechanism of ZMBE for MS is “geometric coverage” effect. The active ingredients in ZMBE can spontaneously adsorb on the MS surface and follow well with the Langmuir isotherm, forming a monolayer adsorption film.
4. The typical components of hydroxycinnamic acid, dimboa, glucuronic acid, and rutin in ZMBE exhibit outstanding electron-sharing abilities, electrostatic attractions, and a synergistic effect based on chemical adsorption and physical adsorption.
5. After protonation, the mixed adsorption is further strengthened. Most of the active ingredients are adsorbed parallel on the Fe (1 1 0) surface. The adsorption capacities of some components such as hydroxycinnamic acid, dimboa, and glucuronic acid will be affected by pH of the corrosive solution, while rutin still provides excellent corrosion inhibition efficiency for MS at different pH solution. Rutin with more aromatic rings, heteroatoms, carbonyls, and hydroxyls displays superior adsorption abilities, with adsorption energy of -375.6 $kcal\cdot mol^{-1}$.
6. The synergistic adsorption effect of multiple components enables ZMBE to be a highly efficient, environmentally friendly, and economically promising corrosion inhibitor in HCl pickling solution.

CRediT authorship contribution statement

Jia-hao Zhu: Writing – review & editing, Writing – original draft. **Bilan Lin:** Writing – review & editing, Funding acquisition. **Tian-hu Duan:** Writing – review & editing. **Han-quan Lin:** Writing – review & editing. **Guo-yu Zhang:** Writing – review & editing. **Xin-xin Zhou:** Writing – review & editing. **Yu-ye Xu:** Writing – review & editing.

Declaration of Competing Interest

The authors declare that they have no known competing financial interests or personal relationships that could have appeared to influence the work reported in this paper.

Acknowledgements

This work was supported by the National Natural Science Foundation of China (Nos. 52178484 and 51408517), and the Xiamen Construction Science and Technology Plan Project (XJK2022-1-22).

References

Abdelaziz, S., Benamira, M., Messaadia, L., Boughoues, Y., Lahmar, H., Boudjerda, A., 2021. Green corrosion inhibition of mild steel in HCl medium using leaves extract of *Arbutus unedo L.* plant: An experimental and computational approach. Colloids Surf. A: Physicochem. Eng. Asp. 619, 126496 https://doi.org/10.1016/j.colsurfa.2021.126496.

Abdullah, H., Anaee, R., Khadom, A., Ali, A., Malik, A., Kadhim, M., 2023. Experimental and theoretical assessments of the chamomile flower extract as a green corrosion inhibitor for aluminum in artificial seawater. Results Phys. 6, 101035 https://doi.org/10.1016/j.rechem.2023.101035.

Ahmed, R., Zhang, S., 2020. Bee pollen extract as an eco-friendly corrosion inhibitor for pure copper in hydrochloric acid. J. Mol. Liq. 316, 113849 https://doi.org/10.1016/j.molliq.2020.113849.

Aihara, J., 1999. Reduced HOMO-LUMO gap as an index of kinetic stability for polycyclic aromatic hydrocarbons. J. Phys. Chem. a. 103, 7487–7495. https://doi.org/10.1021/jp990092i.

Akash, M., Rehman, K., 2020. Ultraviolet-visible (UV-VIS) spectroscopy. Essent. Pharm. Anal. 3, 29–56. https://doi.org/10.1007/978-981-15-1547-7_3.

Akounach, Z., Maofari, A., Damej, M., El-Hajjaji, S., Berisha, A., Mehmeti, V., Labjar, N., Bamaarouf, M., Benmessaoud, M., 2022. Contribution to the corrosion inhibition of aluminum in 1 M HCl by *Pimpinella anisum* extract. Experimental and theoretical studies (DFT, MC, and MD). Int. J. Corros. Scale Inhib. 11 (1), 402–424. https://doi.org/10.17675/2305-6894-2022-11-1-24.

Alemnezhad, M., Ghaffarinejad, A., Omidali, F., 2023. White turnip bark extract as a new green and cost-effective corrosion bio-inhibitor for carbon steel in 1.0 M HCl solution. Chem. Phys. Lett. 831, 140855 https://doi.org/10.1016/j.cplett.2023.140855.

Asfia, M., Rezaei, M., Bahlakeh, G., 2020. Corrosion prevention of AISI 304 stainless steel in hydrochloric acid medium using garlic extract as a green corrosion inhibitor: Electrochemical and theoretical studies. J. Mol. Liq. 315, 113679 https://doi.org/10.1016/j.molliq.2020.113679.

Attou, A., Tourabi, M., Benikdes, A., Benali, O., Ouici, H., Benhiba, F., Zarrouk, A., Jama, C., Bentiss, F., 2020. Experimental studies and computational exploration on the 2-amino-5-(2-methoxyphenyl)-1,3,4-thiadiazole as novel corrosion inhibitor for mild steel in acidic environment. Colloids Surf. a: Physicochem. Eng. Asp. 604, 125320 https://doi.org/10.1016/j.colsurfa.2020.125320.

Bahlakeh, G., Ramezanzadeh, M., Ramezanzadeh, B., 2017. Experimental and theoretical studies of the synergistic inhibition effects between the plant leaves extract (PLE) and zinc salt (ZS) in corrosion control of carbon steel in chloride solution. J. Mol. Liq. 248, 854–870. https://doi.org/10.1016/j.molliq.2017.10.120.

Barrodi, M., Mirzaee, A., Kafashan, A., Zahedifard, S., Majidi, H., Davoodi, A., Hosseinpour, S., 2023. Synergistic effect in *Tragacanth* gum-*Ceftriaxone* hybrid system as an environmentally friendly corrosion inhibitor for mild steel in acidic solutions. Mater. Today Commun. 34, 105390 https://doi.org/10.1016/j.mtcomm.2023.105390.

Bayram, G., Mustafa, K., 2018. Photonic, spectroscopic properties and electronic structure of PTCDI-C8 organic nanostructure. Vib. Spectrosc. 96, 46–51. https://doi.org/10.1016/j.vibspec.2018.02.008.

Bender, R., Feron, D., Mills, D., Ritter, S., Baessler, R., Bettge, D., Graeve, I., Dugstad, A., Grassini, S., Hack, T., 2022. Corrosion challenges towards a sustainable society. Mater. Corros. 73, 1730–1751. https://doi.org/10.1002/maco.202213140.

Berrissoul, A., Ouarhach, A., Benhiba, F., Romane, A., Guenbour, A., Outada, H., Dafali, A., Zarrouk, A., 2021. Exploitation of a new green inhibitor against mild steel corrosion in HCl: Experimental, DFT and MD simulation approach. J. Mol. Liq. 349, 118102 https://doi.org/10.1016/j.molliq.2021.118102.

Berrissoul, A., Ouarhach, A., Benhiba, F., Romane, A., Guenbour, A., Dikici, B., Bentiss, F., Zarrouk, A., Dafali, A., 2022. Assessment of corrosion inhibition performance of *Origanum compactum* extract for mild steel in 1 M HCl: Weight loss, electrochemical, SEM/EDX, XPS, DFT and molecular dynamic simulation. Ind. Crops Prod. 187, 115310 https://doi.org/10.1016/j.indcrop.2022.115310.

Bhardwaj, N., Sharma, P., Guo, L., Dagdag, O., Kumar, V., 2021. Molecular dynamic simulation, quantum chemical calculation and electrochemical behaviour of *Punica granatum* peel extract as eco-friendly corrosion inhibitor for stainless steel (SS-410) in acidic medium. J. Mol. Liq. 346, 118237 https://doi.org/10.1016/j.molliq.2021.118237.

Bouanis, M., Tourabi, M., Nyassi, A., Zarrouk, A., Jama, C., Bentiss, F., 2016. Corrosion inhibition performance of 2,5-bis(4-dimethylaminophenyl)-1,3,4-oxadiazole for carbon steel in HCl solution: Gravimetric, electrochemical and XPS studies. Appl. Surf. Sci. 389, 952–966. https://doi.org/10.1016/j.apsusc.2016.07.115.

Capocchi, A., Bottega, S., Spanò, C., Fontanini, D., 2017. Phytochemicals and antioxidant capacity in four Italian traditional *maize (Zea mays L.*) varieties. Int. J. Food Sci. Nutr. 68 (5), 515–524. https://doi.org/10.1080/09637486.2016.1261809.

Chaudhary, R., Juneja, H., Gharpure, M., 2012. Thermal degradation behaviour of some metal chelate polymer compounds with bis(bidentate) ligand by TG/DTG/DTA. J. Therm. Anal. Calorim. 112, 637–647. https://doi.org/10.1007/s10973-012-2616-8.

Chaudhary, R., Juneja, H., Gandhare, N., 2013. Evaluation of kinetic parameters from TG/DTG data of chelate polymer compounds of isophthaoyl bis (paramethoxyphenylcarbamide). J. Chin. Adv. Mater. Soc. 1 (4), 305–316. https://doi.org/10.1080/22243682.2013.871210.

Chaudhary, R., Ali, P., Gandhare, N., Tanna, J., Juneja, H., 2016. Thermal decomposition kinetics of some transition metal coordination polymers of fumaroyl bis (paramethoxyphenylcarbamide) using DTG/DTA techniques. Arab. J. Chem. 12 (7), 1070–1082. https://doi.org/10.1016/j.arabjc.2016.03.008.

Chen, S., Zhang, H., Qiang, Y., Tan, B., Wu, Y., Chen, S., 2023. Self-assembled monolayers of *Ginkgo biloba exocarp* extract for corrosion protection of copper. J. Mol. Liq. 382, 121941 https://doi.org/10.1016/j.molliq.2023.121941.

Cunha, J., Evangelista, B., Xavier, A., Silva, T., Oliveira, S., Araujo, J., Archanjo, B., Machado, S., Rezende, M., Almeida, T., Mattos, O., D' Elia, E., 2023. Study of furfural derivatives as a possible green corrosion inhibitor for mild steel in CO$_2$-saturated formation water. Corros. Sci. 212, 110907 https://doi.org/10.1016/j.corsci.2022.110907.

Damej, M., Molhi, A., Lgaz, H., Hsissou, R., Aslam, J., Benmessaoud, M., Rezki, N., Lee, H., Lee, W., 2023. Performance and interaction mechanism of a new highly efficient benzimidazole-based epoxy resin for corrosion inhibition of carbon steel in HCl: A study based on experimental and first-principles DFTB simulations. J. Mol. Struct. 1273, 134232 https://doi.org/10.1016/j.molstruc.2022.134232.

Dehghani, A., Bahlakeh, G., Ramezanzadeh, B., 2019a. Green *Eucalyptus* leaf extract: A potent source of bio-active corrosion inhibitors for mild steel. Bioelectrochem. 130, 107339 https://doi.org/10.1016/j.bioelechem.2019.107339.

Dehghani, A., Bahlakeh, G., Ramezanzadeh, B., Ramezanzadeh, M., 2019b. Potential of *Borage* flower aqueous extract as an environmentally sustainable corrosion inhibitor for acid corrosion of mild steel: Electrochemical and theoretical studies. J. Mol. Liq. 277, 895–911. https://doi.org/10.1016/j.molliq.2019.01.008.

Devi, A., Singhal, A., Gupta, R., Prasad, P., 2014. A study on treatment methods of spent pickling liquor generated by pickling process of steel. Clean Techn. Environ. Policy. 16, 1515–1527. https://doi.org/10.1007/s10098-014-0726-7.

Deyab, M., Mohsen, Q., Guo, L., 2022. *Aesculus hippocastanum* seeds extract as eco-friendly corrosion inhibitor for desalination plants: Experimental and theoretical studies. J. Mol. Liq. 361, 119594 https://doi.org/10.1016/j.molliq.2022.119594.

Didouh, H., Buyuksagis, A., Mohammed, M., Dilek, M., Kayali, Y., Suleiman, R., Saleh, T., 2023. Investigating the use of *Moringa oleifera* leaf extract as an environment-friendly corrosion inhibitor for API 5L X52 Steel in 1 M HCl. J. Mol. Liq. 390, 122910 https://doi.org/10.1016/j.molliq.2023.122910.

Du, P., Deng, S., Li, X., 2022. *Mikania micrantha* extract as a novel inhibitor for the corrosion of cold rolled steel in Cl$_2$HCCOOH solution. J. Mater. Res. Technol. 19, 2526–2545. https://doi.org/10.1016/j.jmrt.2022.06.026.

Du, P., Deng, S., Du, G., Shao, D., Xu, D., Li, X., 2023. Synergistic inhibition effect of *Mikania micrantha* extract with potassium iodide on the corrosion of cold rolled steel in methanesulfonic acid solution. Corros. Sci. 220, 111296 https://doi.org/10.1016/j.corsci.2023.111296.

Dutta, A., Saha, S., Adhikari, U., Banerjee, P., Sukul, D., 2017. Effect of substitution on corrosion inhibition properties of 2-(substituted phenyl) benzimidazole derivatives on mild steel in 1 M HCl solution: A combined experimental and theoretical approach. Corros. Sci. 123, 256–266. https://doi.org/10.1016/j.corsci.2017.04.017.

Ech-chebab, A., Missioui, M., Guo, L., El-Khouja, O., Lachhab, R., Kharbouch, O., Galai, M., Ouakki, M., Ejbouh, A., Dahmani, K., Dkhireche, N., Touhami, M., 2022. Evaluation of quinoxaline-2(1H)-one, derivatives as corrosion inhibitors for mild steel in 1.0 M acidic media: Electrochemistry, quantum calculations, dynamic simulations, and surface analysis. Chem. Phys. Lett. 809, 140156 https://doi.org/10.1016/j.cplett.2022.140156.

Echem, O., Tubonemi, T., Chukwuike, V., 2023. Probing the corrosion inhibition efficiency of corn cob extract on aluminium in 1.0 M H$_2$SO$_4$ descaling solution. J. Appl. Sci. Environ. Manage. 27 (6), 1281–1290. https://doi.org/10.4314/jasem.v27i6.32.

El-Azzouzi, M., Azzaoui, K., Warad, I., Hammouti, B., Shityakov, S., Sabbahi, R., Saoiabi, S., Youssoufi, M., Akartasse, N., Jodeh, S., Lamhamdi, A., Zarrouk, A., 2022. *Moroccan*, *Mauritania*, and *Senegalese* gum Arabic variants as green corrosion inhibitors for mild steel in HCl: Weight loss, electrochemical, AFM and XPS studies. J. Mol. Liq. 347, 118354 https://doi.org/10.1016/j.molliq.2021.118354.

El-Faydy, M., Benhiba, F., Warad, I., Saoiabi, S., Alharbi, A., Alluhaybi, A., Lakhrissi, B., Abdallah, M., Zarrouk, A., 2022. Bisquinoline analogs as corrosion inhibitors for carbon steel in acidic electrolyte: Experimental, DFT, and molecular dynamics simulation approaches. J. Mol. Struct. 1265, 133389 https://doi.org/10.1016/j.molstruc.2022.133389.

El-Labban, H., Mahmoud, E., Algahtani, A., 2016. Microstructure, wear, and corrosion characteristics of TiC-laser surface cladding on low-carbon steel. Metall. Mater. Trans. b. 47, 974–982. https://doi.org/10.1007/s11663-016-0602-4.

El-Mokadem, T., Hashem, A., Nour, E., El-Sattar, A., Dawood, E., Abdelshafi, N., 2023. Green synthesis, electrochemical, DFT studies and MD simulation of novel synthesized thiourea derivatives on carbon steel corrosion inhibition in 1.0 M HCl. J. Mol. Struct. 1274, 134567.doi: 10.1016/j.molstruc.2022.134567.

Erfan, K., Mardali, Y., 2024. A study of *Pomegranate* peel extract effect on corrosion inhibition performance on aluminum in HNO$_3$ solution. Colloids Surf. a: Physicochem. Eng. Aspects. 694, 134080 https://doi.org/10.1016/j.colsurfa.2024.134080.

Fatima, B., Aimad, M., Houda, L., Mohammed, B., Malika, S., Mohamme, E., El-Mostapha, L., Souad, E., Najoua, L., 2020. Combination effect of hydro-alcoholic extract of spent coffee grounds (HECG) and potassium Iodide (KI) on the C38 steel corrosion inhibition in 1M HCl medium: Experimental design by response surface methodology. Chem. Data Collect. 29, 100499 https://doi.org/10.1016/j.cdc.2020.100499.

Fergachi, O., Benhiba, F., Rbaa, M., Ouakki, M., Galai, M., Touir, R., Lakhrissi, B., Oudda, H., Touhami, M., 2019. Corrosion inhibition of ordinary steel in 5.0 M HCl medium by benzimidazole derivatives: Electrochemical, UV-Visible spectrometry, and DFT calculations. J. Bio. Tribo. Corros. 5, 21. https://doi.org/10.1007/s40735-018-0215-3.

Fernandes, C., Ferreira, F.T., Nazir, E., Talita, S., Garrett, R., Borges, R., Muricy, G., Valverde, A., Ponzio, E., 2019. *Ircinia strobilina* crude extract as corrosion inhibitor for mild steel in acid medium. Electrochim. Acta. 312, 137–148. https://doi.org/10.1016/j.electacta.2019.04.148.

Fernandez-Aulis, F., Hernandez-Vazquez, L., Aguilar-Osorio, G., Arrieta-Baez, D., Navarro-Ocana, A., 2019. Extraction and identification of anthocyanins in corn cob and corn husk from *Cacahuacintle maize*. J. Food Sci. 84, 954–962. https://doi.org/10.1111/1750-3841.14589.

Garai, S., Garai, S., Jaisankar, P., Singh, J., Elango, A., 2012. A comprehensive study on crude methanolic extract of *Artemisia pallens (Asteraceae*) and its active component as effective corrosion inhibitors of mild steel in acid solution. Corros. Sci. 60, 193–204. https://doi.org/10.1016/j.corsci.2012.03.036.

Goel, R., Siddiqi, W., Ahmed, B., Khan, M., Chaubey, V., 2010. Synthesis characterization and corrosion inhibition efficiency of N-C2 (2E)-2-[4-(dimethylamino) benzylidene] hydrazinyl 2-oxo ethyl benzamide on mild steel. Desalination 263, 45–57. https://doi.org/10.1016/j.desal.2010.06.033.

Gu, T., Xu, Z., Zheng, X., Fu, A., Zhang, F., Al-Zaqri, N., Chen, J., Tan, B., Li, W., 2023. *Lycium barbarum* leaf extract as biodegradable corrosion inhibitor for copper in sulfuric acid medium. Ind. Crops Prod. 203, 117181 https://doi.org/10.1016/j.indcrop.2023.117181.

Haldhar, R., Prasad, D., Nguyen, L., Kaya, S., Bahadur, I., Dagdag, O., Kim, C., 2021. Corrosion inhibition, surface adsorption and computational studies of *Swertia chirata* extract: A sustainable and green approach. Mater. Chem. Phys. 267, 124613 https://doi.org/10.1016/j.matchemphys.2021.124613.

Harb, M., Abubshait, S., Etteyeb, N., Kamoun, M., Dhouib, A., 2020. Olive leaf extract as a green corrosion inhibitor of reinforced concrete contaminated with seawater. Arab. J. Chem. 13, 4846–4856. https://doi.org/10.1016/j.arabjc.2020.01.016.

Hashim, N., Anouar, E., Kassim, K., Zaki, H., Alharthi, A., Embong, Z., 2019. XPS and DFT investigations of corrosion inhibition of substituted benzylidene Schiff bases on mild steel in hydrochloric acid. Appl. Surf. Sci. 476, 861–877. https://doi.org/10.1016/j.apsusc.2019.01.149.

Hou, B., Zhang, Q., Li, Y., Zhu, G., Lei, Y., Wang, X., Liu, H., Zhang, G., 2021. In-depth insight into the inhibition mechanism of pyrimidine derivatives on the corrosion of carbon steel in CO$_2$-containing environment based on experiments and theoretical calculations. Corros. Sci. 181, 109236 https://doi.org/10.1016/j.corsci.2021.109236.

Hu, Z., Meng, Y., Ma, X., Zhu, H., Li, J., Li, C., Cao, D., 2016. Experimental and theoretical studies of benzothiazole derivatives as corrosion inhibitors for carbon steel in 1 M HCl. Corros. Sci. 112, 563–575. https://doi.org/10.1016/j.corsci.2016.08.012.

Hu, J., Xiong, Q., Chen, L., Zhang, C., Zheng, Z., Geng, S., Yang, Z., Zhong, X., 2021. Corrosion inhibitor in CO$_2$-O$_2$-containing environment: Inhibition effect and mechanisms of bis(2-ehylhexyl) phosphate for the corrosion of carbon steel. Corros. Sci. 179, 109173 https://doi.org/10.1016/j.corsci.2020.109173.

Hu, K., Zhuang, J., Ding, J., Ma, Z., Wang, F., Zeng, X., 2017. Influence of biomacromolecule DNA corrosion inhibitor on carbon steel. Corros. Sci. 125, 68–76. https://doi.org/10.1016/j.corsci.2017.06.004.

Huang, L., Zhao, Q., Li, H., Wang, J., Wang, X., Wu, Y., 2022. Investigation of adsorption and corrosion inhibition property of *Hyperoside* as a novel corrosion inhibitor for Q235 steel in HCl medium. J. Mol. Liq. 364, 120009 https://doi.org/10.1016/j.molliq.2022.120009.

Jero, D., Caussé, N., Marsan, O., Buffeteau, T., Chaussec, F., Buvignier, A., Roy, M., Pébère, N., 2023. Film-forming amines adsorption and corrosion kinetics on carbon steel surface in neutral solution investigated by EIS and PM-IRRAS analysis. Electrochim. Acta 443, 141925. https://doi.org/10.1016/j.electacta.2023.141925.

Jian, Z., Duan, J., Zeng, X., Li, Y., Dong, C., Zhang, G., 2023. Unveiling the adsorption and inhibition mechanism of thiadiazole derivatives for mild steel corrosion in hydrochloric acid based on experimental approaches and first-principles calculations. Corros. Sci. 224, 111492 https://doi.org/10.1016/j.corsci.2023.111492.

Jmiai, A., El-Ibrahimi, B., Tara, A., Chadili, M., El-Issami, S., Jbara, O., Khallaayoun, A., Bazzi, L., 2018. Application of *Zizyphus lotuse* - pulp of *Jujube* extract as green and promising corrosion inhibitor for copper in acidic medium. J. Mol. Liq. 268, 102–113. https://doi.org/10.1016/j.molliq.2018.06.091.

Jokar, M., Farahani, T., Ramezanzadeh, B., 2016. Electrochemical and surface characterizations of *Morus alba pendula* leaves extract (MAPLE) as a green corrosion inhibitor for steel in 1 M HCl. J. Taiwan Inst. Chem. Eng. 63, 436–452. https://doi.org/10.1016/j.jtice.2016.02.027.

Jyothi, S., Ravichandran, J., 2014. Corrosion inhibition of mild steel in sulphuric acid using *Luffa aegyptiaca* leaves extract. Acta Metall. Sin. (engl. Lett.) 27 (6), 969–980. https://doi.org/10.1007/s40195-014-0107-6.

Kaya, S., Kaya, C., 2015. A new method for calculation of molecular hardness: A theoretical study. Comput. Theor. Chem. 1060, 66–70. https://doi.org/10.1016/j.comptc.2015.03.004.

Kellal, R., Benmessaoud, D., Safi, Z., Wazzan, N., Al-Qurashi, O., Zertoubi, M., 2023. A new approach for the evaluation of liquid waste generated from plant extraction process for the corrosion mitigation of carbon steel in acidic medium: Case of *Chrysanthemum Coronarium* stems. J. Ind. Eng. Chem. 125, 370–389. https://doi.org/10.1016/j.jiec.2023.05.046.

Khadija, D., Mouhsine, G., Adil, E., Nabil, A., Moussa, O., Amr, E., Rabab, E., Seong-Cheol, E., Mohamed, E., Mohamed, C., 2023. Investigating the inhibitory properties of *Cupressus sempervirens* extract against copper corrosion in 0.5 M $_H2S_O4$: Combining quantum (density functional theory calculation−Monte carlo simulation) and electrochemical-surface studies. ACS Omega 8, 24218–24232. https://doi.org/10.1021/acsomega.3c00589.

Khadom, A., Kadhim, M., Anaee, R., Mahood, H., Mahdi, M., Salman, A., 2021. Theoritical evaluation of *Citrus aurantium* leaf extract as green inhibitor for chemical and biological corrosion of mild steel in acidic solution: Statistical, molecular dynamics, docking, and quantum mechanics study. J. Mol. Liq. 343, 116978 https://doi.org/10.1016/j.molliq.2021.116978.

Kisa, L., 2016. Responses of the phenolic compounds of *Zea mays* under heavy metal stress. Appl. Biol. Chem. 59, 813–820. https://doi.org/10.1007/s13765-016-0229-9.

Kopsell, D., Armel, G., Abney, K., Vargas, J., Brosnan, J., Kopsell, D., 2011. Leaf tissue pigments and chlorophyll fluorescence parameters vary among sweet corn genotypes of differential herbicide sensitivity. Pestic. Biochem. Physiol. 99, 194–199. https://doi.org/10.1016/j.pestbp.2010.12.004.

Kumar, H., Yadav, V., Kumari, A., 2022. Adsorption, corrosion inhibition mechanism, and computational studies of *Azadirachta indica* extract for protecting mild steel: Sustainable and green approach. J. Phys. Chem. Solids 165, 110690. https://doi.org/10.1016/j.jpcs.2022.110690.

Lgaz, H., Lee, H., 2024. Interfacial adsorption mechanism of hydroxycinnamic acids on iron surfaces: A computational perspective toward eco-friendly corrosion mitigation strategies. Appl. Surf. Sci. 644, 158763 https://doi.org/10.1016/j.apsusc.2023.158763.

Li, J., Liu, X., Dong, F., Xu, J., Guo, L., Kong, Z., Tian, Y., Wu, Y., Zheng, Y., 2013. A simple method for the isolation and purification of 2, 4-dihydroxy-7-methoxy-2H-1, 4-benzoxazin-3(4H)-one (DIMBOA) from *Maize* (*Zea mays L.*) seedlings. J. Integr. Agric. 12(1), 95-102. doi: 10.1016/S2095-3119(13)60209-9.

Li, H., Qiang, Y., Zhao, W., Zhang, S., 2021. A green *Brassica oleracea L.* extract as a novel corrosion inhibitor for Q235 steel in two typical acid media. Colloids Surf. a: Physicochem. Eng. Asp. 616, 126077 https://doi.org/10.1016/j.colsurfa.2020.126077.

Li, W., Tan, B., Zhang, S., Guo, L., Ji, J., Yan, M., Wang, R., 2022. Insights into triazole derivatives as potential corrosion inhibitors in CMP process: Experimental evaluation and theoretical analysis. Appl. Surf. Sci. 602, 154165 https://doi.org/10.1016/j.apsusc.2022.154165.

Lima, K., Paiva, V., Perrone, D., Ripper, B., Simões, G., Rocco, M., Veiga, A., D' Elia, E., 2020. *Glycine max* meal extracts as corrosion inhibitor for mild steel in sulphuric acid solution. J. Mater. Res. Technol. 9, 12756–12772. https://doi.org/10.1016/j.jmrt.2020.09.019.

Lin, B., Shao, J., Xu, Y., Lai, Y., Zhao, Z., 2021. Adsorption and corrosion of renewable inhibitor of *Pomelo* peel extract for mild steel in phosphoric acid solution. Arab. J. Chem. 14, 103114 https://doi.org/10.1016/j.arabjc.2021.103114.

Lin, B., Shao, J., Zhao, C., Zhou, X., He, F., Xu, Y., 2023. *Passiflora edulis Sims* peel extract as a renewable corrosion inhibitor for mild steel in phosphoric acid solution. J. Mol. Liq. 375, 121296 https://doi.org/10.1016/j.molliq.2023.121296.

Lin, B., Zhou, X., Duan, T., Zhao, C., Zhu, J., Xu, Y., 2024. Experimental and theoretical study on corrosion inhibition and adsorption performance of *Ipomoea batatas L.* leaf extract for mild steel. Arab. J. Chem. 17, 105410 https://doi.org/10.1016/j.arabjc.2023.105410.

Luo, X., Chenm, B., Li, J., Lan, B., Zhou, C., Ren, Z., Ci, C., Liu, Y., 2023. Synthesis of natural glucomannan derivative as a highly-efficient green inhibitor for mild steel in the simulated seawater. J. Ind. Eng. Chem. 124, 132–146. https://doi.org/10.1016/j.jiec.2023.03.006.

Madaci, A., Ferkous, H., Sedik, A., Delimi, A., Boulechfar, C., Belakhdar, A., Berredjem, M., Chaouch, M.A., Alam, M., Majdoub, H., Jaffrezic-Renault, N., Benguerba, Y., 2023a. Corrosion inhibition, surface adsorption and computational studies of *Swertia chirata* extract: A sustainable and green approach. J. Mol. Liq. 384, 122272 https://doi.org/10.1016/j.molliq.2023.122272.

Madaci, A., Ferkous, H., Sedik, A., Delimi, A., Boulechfar, C., Belakhdar, A., Berredjem, M., Chaouch, M., Alam, M., Majdoub, H., Jaffrezic-Renault, N., Benguerba, Y., 2023b. Experimental and theoretical study of polysaccharides extracted from *Prickly pear nopales pulp* (PPUN) of *Opuntia ficus-indica* as corrosion inhibitors. J. Mol. Liq. 384, 122272 https://doi.org/10.1016/j.molliq.2023.122272.

Martinez-Gonzalez, J., Tello-Salgado, I., Avilés-Flores, M., Landeros-Martínez, L., Flores-De, J., Gonzalez-Rodriguez, J., 2023. Green corrosion and DFT studies of *Ustilago maydis* extract for carbon steel in sulfuric acid. J. Mol. Struct. 1294, 136509 https://doi.org/10.1016/j.molstruc.2023.136509.

Mathur, R., Pandey, I., Rai, S., Ji, G., 2023. Ethanol extract of corn husk for mild steel corrosion prevention in saline water. Mater. Today: Proc. https://doi.org/10.1016/j.matpr.2023.01.037.

Mehdi, M., Ghasem, B., Ali, D., Bahram, R., Mohammad, R., 2019. Combined molecular simulation, DFT computation and electrochemical studies of the mild steel corrosion protection against NaCl solution using aqueous *Eucalyptus* leaves extract molecules linked with zinc ions. J. Mol. Liq. 294, 111550 https://doi.org/10.1016/j.molliq.2019.111550.

Melian, R., Radi, M., Hachimi, F., Galai, M., Ouakki, M., El-Assiri, E., Guo, L., Dkhirche, N., Touhami, M., 2023. Detailed experimental and computational explorations of two heterocyclic compounds as corrosion inhibitors for aluminum alloy 2024–T3 in 3.5% NaCl: Electrochemical/surface studies, DFT/MD modeling. Inorg. Chem. Commun. 152, 110679 https://doi.org/10.1016/j.inoche.2023.110679.

Moradia, A., Ranjbara, Z., Guo, L., Javadpoura, S., Chang, J., 2021. DFT calculations, molecular simulations, and electrochemical investigations of nature-inspired phytochemical attributes of *Achillea millefolium* plants for the construction of effective zinc-based organic anti-corrosion layer on carbon steel. J. Taiwan Inst. Chem. Eng. 129, 273–288. https://doi.org/10.1016/j.jtice.2021.09.035.

Mourya, P., Banerjee, S., Singh, M., 2014. Corrosion inhibition of mild steel in acidic solution by *Tagetes erecta (Marigol*d flower) extract as a green inhibitor. Corros. Sci. 85, 352–363. https://doi.org/10.1016/j.corsci.2014.04.036.

Mrani, S., Ech-Chihbi, E., Salim, R., Daoui, S., Benchat, N., Saffaj, T., Zarrouk, A., Taleb, M., 2023. Experimental, theoretical and MC simulation investigations of the inhibitory efficiency of novel non-toxic pyridazine derivatives inhibition on carbon steel in 1 M HCl solution. J. Mol. Liq. 382, 122043 https://doi.org/10.1016/j.molliq.2023.122043.

Mukhopadhyay, S., Dasgupta, S., Roy, S., Mondal, A., Sukul, D., Ghosal, S., Adhikari, U., 2021. Corrosion inhibition of mild steel by aqueous leaf extract of purple *Hedge* plant: Experimental and theoretical investigation. J. Bio. Tribo. Corros. 7 (4), 139. https://doi.org/10.1007/s40735-021-00577-6.

Mustafa, K., Bayram, G., Fahrettin, G., 2019. Experimental and theoretical studies of the structural, electronic and optical properties of BCzVB organic material. Optik 182, 611–617. https://doi.org/10.1016/j.ijleo.2019.01.080.

Nabajyoti, B., Narendra, N., Asoke, P., 2019. Anti-corrosive properties of quercetin and its derivatives on Fe(111) surface: a quantum chemical approach. SN Appl. Sci. 1, 735. https://doi.org/10.1007/s42452-019-0772-1.

Nadi, I., Belattmania, Z., Sabour, B., Reani, A., Sahibed-dine, A., Jama, C., Bentiss, F., 2019. *Sargassum muticum* extract based on alginate biopolymer as a new efficient biological corrosion inhibitor for carbon steel in hydrochloric acid pickling environment: Gravimetric, electrochemical and surface studies. Int. J. Biol. Macromol. 141, 137–149. https://doi.org/10.1016/j.ijbiomac.2019.08.253.

Nathiya, R., Raj, V., 2017. Evaluation of *Dryopteris cochleata* leaf extracts as green inhibitor for corrosion of aluminium in 1 M H_2SO_4. Egypt. J. Pet. 26, 313–323. https://doi.org/10.1016/j.ejpe.2016.05.002.

Nesane, T., Madala, N., Kabanda, M., Murulana, L., Bahadur, I., 2023. *Lippia javanica* leaf extract as an effective anti-corrosion agent against mild steel corrosion in 1 M HCl and its characterization by UHPLC/Q-TOF-MS spectroscopy and quantum chemical evaluation of its adsorption process on Fe(110). Colloids Surf. a: Physicochem. Eng. Asp. 667, 131405 https://doi.org/10.1016/j.colsurfa.2023.131405.

Obi-Egbedi, N., Obot, I., Umoren, S., 2012. *Spondias mombin L.* as a green corrosion inhibitor for aluminium in sulphuric acid: Correlation between inhibitive effect and electronic properties of extracts major constituents using density functional theory. Arab. J. Chem. 5, 361–373. https://doi.org/10.1016/j.arabjc.2010.09.002.

Obuebite, A., Victor-Oji, C., Eke, W., 2022. Laboratory evaluation of red onion skin extract and its derivative as biomass-based enhanced oil recovery agents. Sci. Afr. 19, e01460.

Olivares-Xometl, O., Likhanova, N., Domínguez-Aguilar, M., Hallen, J., Zamudio, L., Arce, E., 2006. Surface analysis of inhibitor films formed by imidazolines and amides on mild steel in an acidic environment. Appl. Surf. Sci. 252 (6), 2139–2152. https://doi.org/10.1016/j.apsusc.2005.03.178.

Paul, S., Raj, A., Biswas, P., Verma, R., 2014. Tensile flow behavior of ultra low carbon, low carbon and micro alloyed steel sheets for auto application under low to intermediate strain rate. Mater. Des. 57, 211–217. https://doi.org/10.1016/j.matdes.2013.12.047.

Prasad, D., Dagdag, O., Safi, Z., Wazzan, N., Guo, L., 2022. *Cinnamoum tamala* leaves extract highly efficient corrosion bio-inhibitor for low carbon steel: Applying computational and experimental studies. J. Mol. Liq. 347, 118218 https://doi.org/10.1016/j.molliq.2021.118218.

Prasad, D., Maithani, R., El-Ibrahimi, B., 2023. *Mimosa pudica* extract corrosion inhibitive nature for stainless steel in 0.5 mol/L sulfuric acid media. J. Mol. Liq. 389, 122940 https://doi.org/10.1016/j.molliq.2023.122940.

Qiang, Y., Zhang, S., Tan, B., Chen, S., 2018. Evaluation of *Ginkgo* leaf extract as an eco-friendly corrosion inhibitor of X70 steel in HCl solution. Corros. Sci. 133, 6–16. https://doi.org/10.1016/j.corsci.2018.01.008.

Rachid, H., Mouna, A., Fouad, B., Siham, E., Mouhsine, G., Abdelillah, S., Hanane, B., Samir, B., Savas, K., Goncagül, S., Abdelkader, Z., Mohamed, E., Mohamed, R., 2022. Insight of development of two cured epoxy polymer composite coatings as highly protective efficiency for carbon steel in sodium chloride solution: DFT, RDF, FFV and MD approaches. J. Mol. Liq. 360, 119406 https://doi.org/10.1016/j.molliq.2022.119406.

Rahma, E., Ossama, D., Asmae, F., Adil, T., Souad, E., Mohammed, B., Mohammed, M., Mustafa, K., 2023. A strategy to enhance VOC of p-conjugated molecules based on thieno[2,3-b] indole for applications in bulk heterojunction organic solar cells using DFT, TD-DFT, and 3D-QSPR modeling studies. New J. Chem. 47, 812. https://doi.org/10.1039/d2nj04281a.

Rathod, M., Minagalavar, R., Rajappa, S., 2022. Effect of *Artabotrys odoratissimus* extract as an environmentally sustainable inhibitor for mild steel corrosion in 0.5 M H_2SO_4

media. J. Indian Chem. Soc. 99, 100445 https://doi.org/10.1016/j.jics.2022.100445.

Ratna, A., Verma, C., Hossain, S., Gupta, B., Mukhopadhyay, S., 2023. Development of corn husk cellulose reinforced polyvinyl alcohol bio-composite films incorporated with zinc oxide nanoparticles. Bioresour. Technol. Rep. 23, 101570. doi: 10.1016/j.biteb.2023.101570.

Savaş, K., Hassane, L., Abhinay, T., Ashish, K., Dilara, Ö., Nihat, K., Samia, B., 2023. Molecular insights into the corrosion inhibition mechanism of omeprazole and tinidazole: A theoretical investigation. Mol. Simulat. 49, 1632–1646. https://doi.org/10.1080/08927022.2023.2256888.

Scheller, H., Ulvskov, P., 2010. Hemicelluloses. Annu. Rev. Plant Biol. 61, 263–289. https://doi.org/10.1146/annurev-arplant-042809-112315.

Sergio, A., Norma, F., Antonino, P., Manuel, P., Daniel, G., 2010. Computational molecular characterization of the flavonoid rutin. Chem. Cent. J. 4, 12. https://doi.org/10.1186/1752-153X-4-12.

Shadi, S., Bahlakeh, G., Ramezanzadeh, B., Mofidabadi, A., 2023. Experimental and computational exploration of synergistic effect of *Laurus nobilis* extract: Zinc cation on mild steel corrosion inhibition in saline solution. J. Mol. Liq. 385, 122424 https://doi.org/10.1016/j.molliq.2023.122424.

Shahid, A., Sher, B., Latif, U., Aliya, F., Kalsoom, A., Abdullah, M., 2018. Fourier transform infrared spectroscopy: Fundamentals and application in functional groups and nanomaterials characterization. Handbook Mater. Charact. 9, 317–344. https://doi.org/10.1007/978-3-319-92955-2_9.

Shahini, M., Keramatinia, M., Ramezanzadeh, M., Ramezanzadeh, B., Bahlakeh, G., 2021. Combined atomic-scale/DFT-theoretical simulations & electrochemical assessments of the *chamomile* flower extract as a green corrosion inhibitor for mild steel in HCl solution. J. Mol. Liq. 342, 117570 https://doi.org/10.1016/j.molliq.2021.117570.

Shahmoradi, A.R., Talebibahmanbigloo, N., Nickhil, C., Nisha, R., Javidparvar, A., Ghahremani, P., Bahlakeh, G., Ramezanzadeh, B., 2022. Molecular-MD/atomic-DFT theoretical and experimental studies on the *Quince* seed extract corrosion inhibition performance on the acidic-solution attack of mild-steel. J. Mol Liq. 346, 117921 https://doi.org/10.1016/j.molliq.2021.117921.

Sığırcık, G., Yildirim, D., Tüken, T., 2017. Synthesis and inhibitory effect of N, N`-bis (1-phenylethanol) ethylenediamine against steel corrosion in HCl Media. Corros. Sci. 120, 184–193. https://doi.org/10.1016/j.corsci.2017.03.003.

Singh, S., Tambe, S., Gunasekaran, G., Raja, V., Kumar, D., 2008. Electrochemical impedance study of thermally sprayable polyethylene coatings. Corros. Sci. 51, 595–601. https://doi.org/10.1016/j.corsci.2008.11.025.

Singha, A., Ansari, K., Haquec, J., Doharec, P., Lgaz, H., Salghi, R., Quraishi, M., 2017. Effect of electron donating functional groups on corrosion inhibition of mild steel in hydrochloric acid: Experimental and quantum chemical study. J. Taiwan Inst. Chem. Eng. 82, 233–251. https://doi.org/10.1016/j.jtice.2017.09.021.

Sirsendu, S., Manilal, M., Sukdeb, M., Harish, H., Priyabrata, B., 2021. Competitive corrosion inhibition performance of alkyl/acyl substituted 2-(2-hydroxybenzylideneamino) phenol protecting mild steel used in adverse acidic medium: A dual approach analysis using FMOs/molecular dynamics simulation corroborated experimental findings. Colloids Surf. A: Physicochem. Eng. Aspects. 617, 126314 https://doi.org/10.1016/j.colsurfa.2021.126314.

Sukdeb, M., Sourav, B., Priyabrata, B., 2023. Insights into the uses of two azine decorated d10-MOFs for corrosion inhibition application on mild steel surface in saline medium: Experimental as well as theoretical investigation. J. Mol. Liq. 381, 121789 https://doi.org/10.1016/j.molliq.2023.121789.

Sun, A., Cui, G., Liu, Q., 2023a. Capsule corrosion inhibitor loaded with hyperbranched chitosan: Carbon dioxide corrosion protection for downhole pipelines in oil fields. Colloids Surf. a: Physicochem. Eng. Asp. 664, 131106 https://doi.org/10.1016/j.colsurfa.2023.131106.

Sun, X., Qiang, Y., Hou, B., Zhu, H., Tian, H., 2022. Cabbage extract as an eco-friendly corrosion inhibitor for X70 steel in hydrochloric acid medium. J. Mol. Liq. 362, 119733 https://doi.org/10.1016/j.molliq.2022.119733.

Sun, Y., Zhang, Y., Xu, C., Tan, B., Li, W., Zheng, X., Brahmia, A., 2023b. *Honeysuckle* extract as an environment-friendly corrosion inhibitor for copper in sulfuric acid medium. Ind. Crops Prod. 197, 116551 https://doi.org/10.1016/j.indcrop.2023.116551.

Swathi, N., Samshuddin, S., Aljohani, T., Rasheeda, K., Alva, V., Baig, I., Maslamani, N., Alamri, A., 2023. Investigation of some new triazole derivatives for inhibiting the acid corrosion of C1018 carbon steel: Correlation of electrochemical studies with quantum chemical calculations. S. Afr. J. Chem. Eng. 44, 123–134. https://doi.org/10.1016/j.sajce.2023.01.012.

Tachaapaikoon, C., Kyu, K., Ratanakhanokchai, K., 2006. Purification of xylanase from alkaliphilic *Bacillus* sp. K-8 by using corn husk column. Process Biochem. 41, 2441–2445. https://doi.org/10.1016/j.procbio.2006.07.004.

Tan, B., Fu, A., Guo, L., Ran, Y., Xiong, J., Marzouki, R., Li, W., 2023. Insight into anti-corrosion mechanism of *Dalbergia odorifera* leaves extract as a biodegradable inhibitor for X70 steel in sulfuric acid medium. Ind. Crops Prod. 194, 116106 https://doi.org/10.1016/j.indcrop.2022.116106.

Tan, B., Gong, Z., He, W., Xiong, J., Guo, L., Marzouki, R., 2024. Insight into the anti-corrosion mechanism of crop waste *Arachis hypogaea L.* leaf extract for copper in sulfuric acid medium. Sustain. Chem. Pharm. 38, 101449 https://doi.org/10.1016/j.scp.2024.101449.

Tang, M., Deng, S., Du, G., Li, X., 2023. *Mikania micrantha* extract/KI blend as a novel synergistic inhibitor for steel corrosion in concentrated H_3PO_4 solution. Ind. Crops Prod. 193, 116237 https://doi.org/10.1016/j.indcrop.2023.116237.

Thakur, A., Kaya, S., Abousalem, A., Kumar, A., 2022. Experimental, DFT and MC simulation analysis of *Vicia sativa* weed aerial extract as sustainable and eco-benign corrosion inhibitor for mild steel in acidic environment. Sustain. Chem. Pharm. 29, 100785 https://doi.org/10.1016/j.scp.2022.100785.

Thanh, L., Vu, N., Binh, P., Dao, V., Thu, V., Hien, P., Panaitescu, C., Nam, N., 2020. Combined experimental and computational studies on corrosion inhibition of *Houttuynia cordata* leaf extract for steel in HCl medium. J. Mol. Liq. 315, 113787 https://doi.org/10.1016/j.molliq.2020.113787.

Thomas, A., Prajila, M., Shainy, K., Joseph, A., 2020. A green approach to corrosion inhibition of mild steel in hydrochloric acid using fruit rind extract of *Garcinia indica (Binda*). J. Mol. Liq. 312, 113369 https://doi.org/10.1016/j.molliq.2020.113369.

Tian, J., Xu, Y., Song, B., Dong, Y., Wang, Y., 2016. Optimization of cellulase-ultrasound-assisted extraction of quercetin from corn husk. J. Food Saf. Qual. 7 (4), 1667–1673. https://doi.org/10.19812/j.cnki.jfsq11-5956/ts.2016.04.057.

Umoren, S., Suleiman, R., Obot, I., Solomon, M., Adesina, A., 2022. Elucidation of corrosion inhibition property of compounds isolated from Butanolic Date Palm Leaves extract for low carbon steel in 15% HCl solution: Experimental and theoretical approaches. J. Mol. Liq. 356, 119002 https://doi.org/10.1016/j.molliq.2022.119002.

Vaszilcsin, C., Putz, M., Kellenberger, A., Dan, M., 2023. On the evaluation of metal-corrosion inhibitor interactions by adsorption isotherms. J. Mol. Struct. 1286, 135643 https://doi.org/10.1016/j.molstruc.2023.135643.

Vazquez-Olivo, G., López-Martínez, L., Contreras-Angulo, L., Heredia, J., 2019. Antioxidant capacity of lignin and phenolic compounds from corn stover. Waste Biomass Valor. 10, 95–102. https://doi.org/10.1007/s12649-017-0028-5.

Wang, H., Deng, S., Xu, J., Xu, D., Shao, D., Du, G., Li, X., 2023a. Synergistic mixture of *Eupatorium adenophora spreng* stems extract/KI as an efficient inhibitor for the corrosion of steel in H_2SO_4. J. Ind. Eng. Chem. 130, 218–233. https://doi.org/10.1016/j.jiec.2023.09.025.

Wang, J., Shi, P., Du, M., Xu, T., Shan, X., Tian, Z., 2024. Effects of *Alcaligenes sp.* on corrosion inhibition of sulfate-reducing bacteria in oilfield produced water. Corros. Sci. 227, 111771 https://doi.org/10.1016/j.corsci.2023.111771.

Wang, Q., Zhang, Q., Liu, L., Zheng, H., Wu, X., Li, Z., Gao, P., Sun, Y., Yan, Z., Li, X., 2022. Experimental, DFT and MD evaluation of *Nandina domestica Thunb.* extract as green inhibitor for carbon steel corrosion in acidic medium. J. Mol. Struct. 1265, 133367 https://doi.org/10.1016/j.molstruc.2022.133367.

Wang, Q., Zheng, H., Zhao, C., Zhang, Q., Liu, L., Wu, X., Zhang, R., Sun, Y., Yan, Z., Li, X., 2023b. Experimental and theoretical insights into *Oxalis corniculata L.* extract as a sustainable and eco-friendly corrosion inhibitor for carbon steel in acidic environments. Mater. Chem. Phys. 306, 128075 https://doi.org/10.1016/j.matchemphys.2023.128075.

Wu, J., Gao, T., Guo, H., Zhao, L., Lv, S., Lv, J., Yao, R., Yu, Y., Ma, F., 2023. Application of molecular dynamics simulation for exploring the roles of plant biomolecules in promoting environmental health. Sci. Total Environ. 869, 161871 https://doi.org/10.1016/j.scitotenv.2023.161871.

Wu, Y., Zhang, Y., Jiang, Y., Qian, Y., Guo, X., Wang, L., Zhang, J., 2020. Orange peel extracts as biodegradable corrosion inhibitor for magnesium alloy in NaCl solution: Experimental and theoretical studies. J. Taiwan Inst. Chem. Eng. 115, 35–46. https://doi.org/10.1016/j.jtice.2020.10.010.

Xu, C., Tan, B., Zhang, S., Li, W., 2022. Green and sustainable local biomaterials for oilfield chemicals: *Griffonia simplicifolia* extract as steel corrosion inhibitor in hydrochloric acid. J. Taiwan Inst. Chem. Eng. 139, 104532 https://doi.org/10.1016/j.jtice.2022.104532.

Xu, N., Yang, X., Zhang, Q., 2024. Insight into interfacial adsorption and inhibition mechanism of *Aconitum carmichaelii debx* extract as high-efficient corrosion inhibitor for carbon steel in acidic solution. J. Mol. Liq. 393, 123602 https://doi.org/10.1016/j.molliq.2023.123602.

Yoshidaa, M., Aihara, J., 1998. Validity of the weighted HOMO–LUMO energy separation as an index of kinetic stability for fullerenes with up to 120 carbon atoms. Phys. Chem. Chem. Phys. 1, 227–230. https://doi.org/10.1039/a807917j.

Zaidi, K., Bouroumane, N., Merimi, C., Aouiniti, A., Touzani, R., Oussaid, A., Hammouti, B., Salim, R., Kaya, S., Ibrahim, S.M., 2023. Iron-ligand complex, an efficient inhibitor of steel corrosion in hydrochloric acid media. J. Mol. Struct. 1284, 135434 https://doi.org/10.1016/j.molstruc.2023.135434.

Zakaria, F., Hamidon, T., Hussin, M., 2022. *Glycine max* meal extracts as corrosion inhibitor for mild steel in sulphuric acid solution. J. Indian Chem. Soc. 99, 100329 https://doi.org/10.1016/j.jics.2021.100329.

Zeng, W., Xu, Y., Ge, P., Xiao, W., Liu, Q., Gao, Z., Yan, Y., 2023. *Ipomoea batatas* leaves extract as a green corrosion inhibitor for Q235 steel in HCl solution. Int. J. Electrochem. 16, 211031 https://doi.org/10.20964/2021.10.40.

Zhang, M., Guo, L., Zhu, M., Wang, K., Zhang, R., He, Z., Lin, Y., Leng, S., Anadebe, V., Zheng, X., 2021. *Akebia trifoliate koiaz* peels extract as environmentally benign corrosion inhibitor for mild steel in HCl solutions: Integrated experimental and theoretical investigations. J. Ind. Eng. Chem. 110, 227–236. https://doi.org/10.1016/j.jiec.2021.06.009.

Zhang, J., Zhan, F., Ai-Zaqri, N., 2023. Corrosion inhibition performance of *Punica granatum L.* extract on Q235 steel in H_2SO_4 environment: Electrochemical, morphological, and quantum chemical studies. Int. J. Electrochem. Sci. 18, 100267 https://doi.org/10.1016/j.ijoes.2023.100267.

Zhao, C., Lin, B., Zhou, X., Zhu, J., Duan, T., Xu, Y., 2023. Corrosion inhibition and adsorption behavior of *Musa basjoo siebold* leaves extract on mild steel in H_3PO_4 solution: Experimental and theoretical studies. Prot. Met. https://doi.org/10.1134/S2070205123700934.

Zhou, Z., Min, X., Wan, S., Liu, J., Liao, B., Guo, X., 2023. A novel green corrosion inhibitor extracted from waste *Feverfew* root for carbon steel in H_2SO_4 solution. Results. Eng. 17, 100971 https://doi.org/10.1016/j.rineng.2023.100971.

Zuo, X., Li, W., Luo, W., Zhang, X., Qiang, Y., Zhang, J., Li, H., Tan, B., 2021. Research of *Lilium brownii* leaves extract as a commendable and green inhibitor for X70 steel corrosion in hydrochloric acid. J. Mol. Liq. 321, 114914 https://doi.org/10.1016/j.molliq.2020.114914.